

A WIDE-FIELD HUBBLE SPACE TELESCOPE SURVEY OF THE CLUSTER CL 0024+16 AT Z=0.4. III: SPECTROSCOPIC SIGNATURES OF ENVIRONMENTAL EVOLUTION IN EARLY TYPE GALAXIES

SEAN M. MORAN¹, RICHARD S. ELLIS,¹, TOMMASO TREU^{2,3,4}, IAN SMAIL⁵, ALAN DRESSLER⁶, ALISON L. COIL⁷, GRAHAM P. SMITH¹

¹California Institute of Technology, Department of Astronomy, Mail Code 105-24, Pasadena, CA 91125, USA email: smm@astro.caltech.edu,

rse@astro.caltech.edu ²Department of Physics, University of California, Santa Barbara, CA 93106, email: tt@physics.ucsb.edu ³University of California at Los Angeles, Department of Physics & Astronomy, Los Angeles, CA 90095 ⁴Hubble Fellow ⁵Department of Physics, University of Durham, South Road, Durham DH1 3LE, UK. ⁶The Observatories of the Carnegie Institutions of Washington, 813 Santa Barbara St., Pasadena, CA 91101 ⁷Department of Astronomy, University of California, Berkeley, CA 94720

To Appear in ApJ

ABSTRACT

We report results from a panoramic spectroscopic survey of 955 objects in the field of the rich cluster Cl 0024+1654 ($z \simeq 0.4$), complementing the *HST* imaging presented in the first paper in this series. Combining with previous work, we compile a catalog of 1394 unique redshifts in the field of this cluster, including 486 cluster members spread across an area 10 Mpc in diameter. Our new spectroscopic sample includes over 200 high quality spectra of cluster members. We examine the properties of a large sample of 104 cluster early-types as a function of cluster radius and local density, using them as sensitive tracers of the various physical processes that may be responsible for galaxy evolution. By constructing the Fundamental Plane of Cl 0024, we infer an evolution in the mean mass to light ratio of early-types with respect to $z = 0$ of $\Delta < \log(M/L_V) > = -0.14 \pm 0.02$. In the cluster center, we detect a significantly increased scatter in the relationship compared to that seen in local clusters. Moreover, we observe a clear radial trend in the mass to light ratios of individual early types, with the oldest galaxies located in the cluster core. Galaxies are apparently younger at larger radius, with E+S0s in the periphery having M/L_V ratios that nearly match values seen in the field at a similar redshift. The strong radial trend is seen even when the sample is restricted to a narrow range in galaxy mass. Independent spectral indicators used in combination reveal an abrupt interaction with the cluster environment which occurs near the virial radius of Cl 0024, revealed by small bursts of star formation in a population of dim early-types, as well as by enhanced Balmer absorption for a set of larger E+S0s closer to the cluster core. We construct a simple infall model used to compare the timescales and strengths of the observed interactions in this cluster. We examine the possibility that bursts of star formation are triggered when galaxies suffer shocks as they encounter the intra-cluster medium, or by the onset of galaxy harassment.

Subject headings: galaxies: clusters: individual (Cl 0024+1654) — galaxies: elliptical and lenticular, cD — galaxies: evolution — galaxies: formation — galaxies: fundamental parameters — galaxies: kinematics and dynamics

1. INTRODUCTION

Environmental processes have clearly played a significant role in shaping the morphological evolution of galaxies. Butcher & Oemler (1978) first noted the increased fraction of actively-star forming galaxies in cluster cores at redshifts $z \simeq 0.4$ and subsequent studies clarified direct evolution in the relationship between morphological fractions and local density (Dressler et al. 1997). Recent work has extended these measures to galaxy samples in lower density environments and at higher redshifts (Treu et al. 2003; Smith et al. 2005; Postman et al. 2005), delineating a picture where the fraction of early-type (hereafter elliptical and S0) galaxies to some rest-frame luminosity limit grows with time, and at a rate that seems to depend sensitively on the local density.

What processes govern this apparent transformation of star-forming disk and irregular galaxies into the abundant elliptical and S0 population seen in present-day clusters? Galaxy clusters provide excellent laboratories to study these environmental effects, particularly at intermediate redshifts (where the relevant processes were perhaps most active) and over the full range of cluster radii, from the well-mixed cluster core to the outermost regions where field galaxies are falling into the cluster for the first time.

This is the third paper in a series concerned with explor-

ing the origin and evolution of the morphology-density relation via a detailed study of hundreds of galaxies to the turn around radius in the rich cluster Cl 0024+1654 ($z=0.40$). The essential ingredients for this study include a large Hubble Space Telescope WFPC-2 image mosaic providing galaxy morphologies, and Keck spectroscopy, for membership, dynamics and diagnostics of recent star formation activity. In the first paper in the series, Treu et al. (2003, hereafter Paper I), we analyzed the relation between morphology, local density and cluster radius and pinpointed possible environmental processes which curtail star-formation within infalling galaxies. Local density was shown to be a more reliable measure of the environmental trends than cluster radius, suggesting most infalling galaxies retain their original group properties until they reach the Virial radius where such substructure is quickly erased. In the second paper (Kneib et al. 2003), a physical model for the distribution of cluster mass and mass to light ratio was determined from strong and weak gravitational lensing.

In this third paper, we turn now to the spectroscopic diagnostics. Spectroscopy of cluster members at various stages of infall can provide a key to the dominant environmental processes. As introduced in Paper I, different physical mechanisms will produce recognizable spectral and dynamical signatures in the affected galaxies. While several independent

processes can operate simultaneously in the central 0.5–1 Mpc, these can be separated by contrasting differences over a wider dynamic range in radius and local density.

Since our first paper was submitted, we have continued to observe Cl 0024+1654 (hereafter Cl 0024) at the Keck observatory and our goal here is twofold: First, we update and finalize the redshift catalog of cluster members. Using the DEIMOS spectrograph on *Keck II*, we have now obtained spectra for nearly 1000 galaxies to a projected distance of 5 Mpc; the tally of cluster members is nearly 500 galaxies, the largest such sample at intermediate redshift.

Secondly, in addition to measuring redshifts in abundance we have exposed on a brighter subset of known members to a limit where our morphological classifications are particularly reliable. At this limit, our high-quality DEIMOS spectra can be used to examine precise trends observed in various diagnostics of recent star formation as well as resolved dynamics of disk and early-type members. Our goal is to analyze these trends according to both the timescale and physical location over which they occur in order to develop an overall picture of the processes that affect the cluster galaxy population.

Much of course has been learned from detailed spectroscopy of galaxies in intermediate redshift clusters (e.g. Dressler & Gunn 1983; Couch & Sharples 1987; Poggianti et al. 1999, and references therein). However, previous studies of this type have either focused on the cluster core, where morphologies are available or relied on spectral types or colors to trace the effects of environment out to the cluster periphery (Abraham et al. 1996b; Kodama et al. 2001). With a larger sample of morphologies and high quality spectra over the full range of local densities in Cl 0024, we aim to provide a more complete picture of the environmental processes involved and their range of application.

We focus here on cluster members classified as early-type (E+S0) in our morphological catalog (Paper I). In the local universe, cluster early-type galaxies are an extremely homogeneous population in terms of their stellar populations and structural properties (e.g. Dressler et al. 1987; Djorgovski & Davis 1987; Bower et al. 1992; Bender, Burstein, & Faber 1992). Nevertheless, the evolution of the morphology density relation indicates that a substantial fraction was accreted or transformed at intermediate redshift. Several of the proposed environmental mechanisms are thought to have transformed spirals into S0s (Dressler et al. 1997; Fasano et al. 2000; Smith et al. 2005; Postman et al. 2005).

By studying these galaxies at intermediate redshifts and contrasting their spectral properties with those of their counterparts in the field and local universe we expect to be sensitive to signatures of past and current environmental activity. In this sense, we will explore early-type galaxies as “test particles” of recent activity. Building on the conclusions herein, a future paper will address the properties of spiral galaxies in Cl 0024 and discuss the galaxy population as a whole, taking into account morphological evolution (see, e.g., the discussion of *progenitor bias* in van Dokkum & Franx 2001).

The signal/noise of our early-type spectra was designed to be adequate to measure reliable stellar velocity dispersions for each galaxy, enabling us to construct the Fundamental Plane and, in particular, its possible variation with location. This emerges as a powerful probe of variations in the M/L_V ratios and hence the luminosity-weighted ages of the stellar populations. Precise measures of various line diagnostics permit us to independently probe the star formation histories over well-

understood timescales. In combination, both methods allow us to examine the relative importance of the environment and to constrain the physical mechanisms responsible.

A key issue is the relationship between trends found in Cl 0024 at various radii and those found in the field at approximately the same cosmic epoch. To facilitate such a comparison we make use of the recent comprehensive study of 163 field E+S0s undertaken by Treu et al. (2005a,b) in the northern GOODS field.

A plan of the paper follows. In § 2, we summarize the new spectroscopic observations and their data reduction, and present the final catalog of spectroscopic redshifts. In § 3 we discuss our measurements of the stellar velocity dispersions, the fits to the surface photometry, the various spectral line indices, as well as an improved estimate of the local environmental densities. In § 4 we present our results focusing first on the Fundamental Plane and the implications of the scatter and various trends seen as a function of luminosity and location, and correlations between the Balmer absorption and metal line strengths with the velocity dispersion. We also analyze both radial trends and those seen in the residuals from our global cluster and field relations. In § 5, we develop an integrated picture which combines these independent methods and discuss this in the light of the conclusions we drew in Paper I. For consistency, throughout this series of papers we use the cosmology adopted in Paper I ($H_0 = 65.0 \text{ km s}^{-1}$, $\Omega_m = 0.3$, $\Omega_\Lambda = 0.7$).

2. OBSERVATIONS

2.1. Imaging

High resolution imaging of Cl 0024 is crucial for the type of spectroscopic study we wish to undertake, both for the purpose of selecting a sample of E+S0 galaxies, and to allow us to analyze the surface photometry of the selected galaxies.

Paper I presented the results of a wide-field *HST* imaging survey of Cl 0024. The survey includes a sparsely-sampled mosaic of 39 WFPC2 images taken in the F814W filter ($\sim I$ band), providing good coverage of the cluster field out to radius $> 5 \text{ Mpc}$ ($\sim 14'$). Paper I reported morphological classifications down to $I = 22.5$. Classifications to a limiting magnitude of $I = 21.1$ were found to be very reliable, in that several authors, working independently, agreed upon the morphology for most objects. This included differentiation between the sub-types E, E/S0, and S0. While ellipticals and S0s were grouped together for the purposes of Paper I, it is useful in this paper to detect any differences between the populations of Es and S0s: if spirals are actively transforming into S0s at $z \sim 0.4$, we might expect to detect differences in the stellar populations of the two groups.

Although face-on S0s are notoriously hard to distinguish from ellipticals, especially at high redshift where S0 disks may be too dim to detect (Smail et al. 1997; Fabricant et al. 2000), we can partially avoid this difficulty by focusing on the brightest early type galaxies where all but the faintest disks should be detectable. In this paper, therefore, we will report distinctions between E, E/S0, and S0 galaxies for a brighter subset of this sample, to $I = 21.1$. We additionally employ a technique not discussed in Paper I, namely that based on the residual signals found after subtraction of an axisymmetric de Vaucouleurs profile (§3.3 and 4.1.1).

2.2. Spectroscopy

Designed to both identify cluster members and acquire high signal to noise spectra of galaxies in Cl 0024, we began our

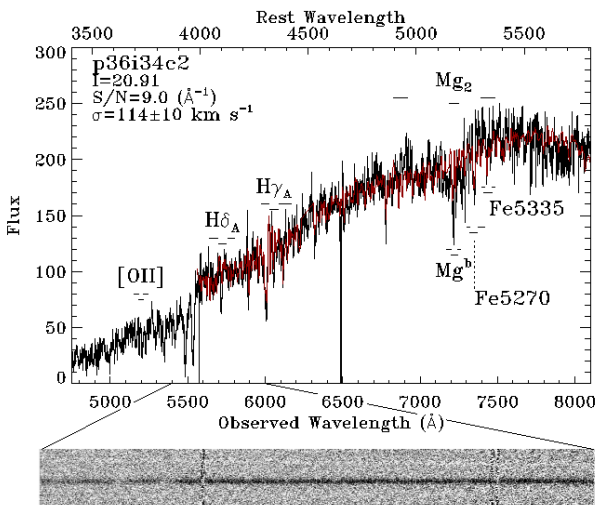


FIG. 1.— A typical spectrum for a galaxy near the magnitude limit of our brighter sample. The entire 1D spectrum is plotted at top, with a segment of the 2D spectrum displayed below it. We have measured equivalent widths for the spectral lines indicated. The pseudo-continuum and index bandpasses used for each index are marked. Overplotted in red is the best-fit template spectrum used in measuring the stellar velocity dispersion, for the full spectral range where it overlaps with our galaxy spectrum. The resulting velocity dispersion is $\sigma = 114 \pm 10 \text{ km s}^{-1}$.

spectroscopic campaign in October 2001 with LRIS on *Keck I*. While some observations were completed that year (see Paper I), poor weather forced us to return in October 2002 and again in October 2003, this time making use of the new DEIMOS spectrograph on *Keck II* (Faber et al. 2003). The survey was largely completed in 2003, though a small number of additional galaxies were observed in December 2004. In total, we have obtained new spectra of 955 objects, including 261 confirmed cluster members to $I = 22.5$.

Spectroscopic targets were selected from the CFHT I -band mosaic of the Cl 0024 field (Czoske et al. 2002). In designing slit masks, selection priority was given to known cluster members with *HST* morphologies, followed by galaxies in the *HST* survey without a known redshift, to $I = 22.5$. Galaxies without *HST* images filled the remainder of each slit mask, with priority given to known members. All targeted galaxies were brighter than $I = 22.5$. Masks were designed so as to provide good coverage across the Cl 0024 field, while also maximizing the number of known-member spiral galaxies that could be observed with tilted slits (for extracting rotation curves from extended line emission; to be discussed in a later paper.)

We observed a total of 12 DEIMOS slit masks in 2002 and 2003, covering the entire field of the HST mosaic. We employed the 900 line/mm grating, with a central wavelength of 6200 Å. This setup provides spectral coverage from 4500 to 8000 Å, with a pixel scale of approximately $0.^{\prime\prime}12 \times 0.44 \text{ Å}$. Slitlets were milled to be $1''$ wide, providing spectral resolution of $\sigma \sim 50 \text{ km s}^{-1}$. For most masks, the exposure time was 2.5 hrs (5×1800 s), though four masks were only observed for 2 hrs (4×1800 s). In December 2004, we observed a single additional mask for 3 hrs, 10 min, (5×1200 s plus 3×1800 s) with the 600 line/mm grating, providing resolution of $\sim 70 \text{ km s}^{-1}$. The central wavelength was again 6200 Å, providing similar spectral coverage. In 2002, conditions were fairly poor, with thin clouds frequently interrupting

observations. Seeing was approximately $0.^{\prime\prime}7$. In 2003, seeing was good ($0.^{\prime\prime}5$ – $0.^{\prime\prime}6$), though conditions were not photometric. And in 2004, conditions were generally good, with seeing varying between $0.^{\prime\prime}7$ – $1.^{\prime\prime}1$ across three nights.

We analyze data for 104 E+S0 galaxies, of which 71 have particularly high quality spectra (generally defined in this paper to be those for which reliable stellar velocity dispersions were measured). Twelve of these E+S0s (6 high quality) come from the LRIS observations discussed in Paper I, with the remainder from DEIMOS. Broken down by specific morphological type, our sample includes 34 galaxies classified as E, 50 as S0, and 20 as E/S0. Of the galaxies with high quality spectra available, 27 are E, 38 S0, and 10 E/S0.

We designed our spectroscopic campaign to yield high quality spectra for galaxies brighter than $I = 21.1$, in order to match the magnitude limit of Paper I for precise morphological classification. As expected, all objects where we have obtained high quality spectra are brighter than this limit. We therefore divide our E+S0 galaxies into a sample that is brighter than $I = 21.1$ and one that includes all observed E+S0 members down to $I = 22.5$. For the larger sample, signal/noise is generally sufficient to measure and examine trends in spectral line strengths. An M_V^* galaxy in Cl 0024 corresponds to $I = 19.5$ (Smail et al. 1997, Paper I), such that our two samples represent galaxies brighter than $M_V^* + 1.6$ and $M_V^* + 3.0$, respectively.

2.2.1. Data Reduction

Spectra were reduced using the DEEP2 DEIMOS data pipeline¹ (Davis et al. 2003). The pipeline performs bias removal, flat-fielding, and cosmic-ray rejection. It then separates slitlets and performs wavelength calibration and sky subtraction. For wavelength calibration, the pipeline uses an optical model of the DEIMOS mask to generate an initial wavelength solution. Arc-lamp frames, consisting of 1s exposures with Ne, Ar, Kr, and Xe lamps, are then used to refine the calibration.

From the reduced two-dimensional spectra, the pipeline extracts one-dimensional spectra using either a variance-weighted boxcar function, or a variant of the optimal extraction method described by Horne (1986). We perform our analysis on spectra extracted via the boxcar method, though the difference using the optimal extraction is minimal. Figure 1 presents a 1D reduced spectrum of a galaxy that is near the magnitude limit of our brighter sample, along with a portion of the reduced 2D spectrum for the same object.

For LRIS data, individual slitlets were separated and reduced in a standard manner (see, e.g., Treu et al. 1999, 2001b).

For each reduced spectrum, redshifts were determined by examining the spectra to identify key absorption and emission lines. We obtained initial redshift guesses via automated fitting of template stellar spectra to each object spectrum. Each spectrum was then judged by eye to determine the correct redshift. Most redshifts were identified by SMM, and checked by TT. Table 1 lists the basic properties of the sample of 104 E+S0 galaxies. In later tables, galaxies will be referred to by the object name listed here.

2.2.2. Cl 0024 Redshift Catalog

As in Paper I, we combine our new spectroscopy with data from previous surveys (Czoske et al. 2001; Dressler et al.

¹ Software available at <http://astron.berkeley.edu/~cooper/deep/spec2d>

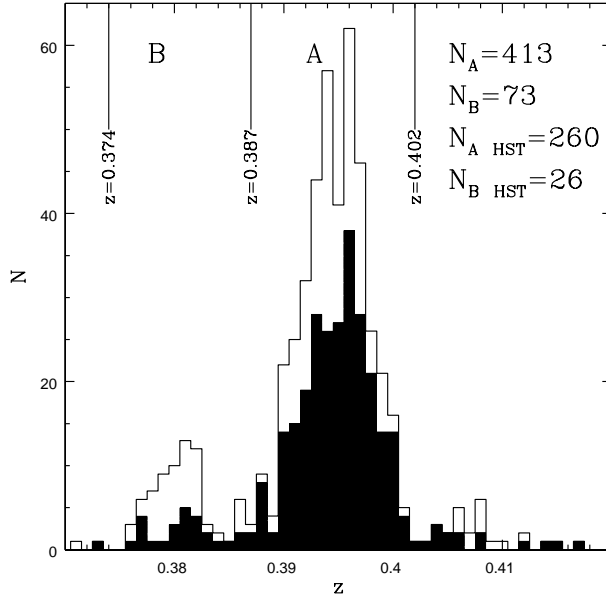


FIG. 2.— Redshift distribution of galaxies in the field of Cl 0024 in the vicinity of $z \sim 0.4$. From Paper I, updated to include the final tally of redshifts in our Keck spectroscopic campaign. The empty histogram reflects all known members, while the shaded histogram represents members present in the HST mosaic of Paper I. The two peaks in the distribution are discussed by Czoske et al. (2002).

1999) to compile a comprehensive redshift catalog of objects in the Cl 0024 field. In total, we have compiled a catalog with 1394 redshifts of unique objects, of which 486 are cluster members. Table 2 presents an excerpt from the total redshift catalog, which is available in its entirety online. Approximately sixty unique redshifts were kindly provided by D. Koo & A. Metevier. These are omitted from Table 2 (reducing the tally to 1334 objects) and will be published separately by Metevier et al. (2005, in preparation). A final merged catalog will be available from the two groups' websites. As in Paper I and Czoske et al. (2002), we define a cluster member to be a galaxy that lies in either Peak A or Peak B of the cluster, as illustrated in Figure 2. This encompasses a redshift range from $z = 0.374$ to $z = 0.402$.

While Table 2 includes galaxies from across the entire field of Cl 0024, our sample of E+S0 galaxies is drawn from the area imaged by WFPC2, so we are particularly concerned with the distribution of known redshifts within the area of the *HST* survey. To draw firm conclusions about the early type population of Cl 0024, we must draw our E+S0 galaxies from a sample that is sufficiently complete and representative of the population as a whole.

We define the redshift completeness of the catalog, as a function of magnitude or cluster radius, as the number of objects with identified redshifts divided by the total number of objects in the *HST* imaging catalog (See Paper I). Completeness has naturally increased from the values given in Paper I; ignoring objects brighter than the brightest cluster galaxy ($I = 17.75$), it is now $\sim 65\%$ for $17.75 < I < 21.1$ and $\sim 40\%$ for $17.75 < I < 22.5$. Importantly for this work, our coverage of E+S0 galaxies within 3 Mpc of the cluster center is particularly high. Within this radius, Figure 3 shows that we have identified redshifts for over 80% of E+S0 galaxies

TABLE 2
CL 0024+1654 REDSHIFT CATALOG

α ($^{\circ}$)	δ ($^{\circ}$)	z_{best}	Quality ^a	Source ^b	$\langle z \rangle$	δz	N_z
6.845741	17.133789	0.3940	0	2	0.3940	0.0000	1
6.837580	16.997200	0.3966	1	1	0.3964	0.0004	2
6.827622	17.378466	0.3792	0	2	0.3792	0.0000	1
6.821529	17.200779	0.3758	0	2	0.3758	0.0000	1
6.812725	17.213043	0.3813	0	2	0.3813	0.0000	1
6.801040	17.199699	0.3955	1	5	0.3955	0.0001	2
6.765210	17.191099	0.3955	1	5	0.3956	0.0002	3
6.759056	17.073933	0.3790	0	2	0.3790	0.0000	1
6.744001	17.070641	0.3940	0	2	0.3940	0.0000	1
6.737525	17.066620	0.1870	2	3	0.1870	0.0000	1
...							

NOTE. — The complete version of this table is in the electronic edition of the Journal. The printed edition contains only a sample. Explanation of columns: z_{best} , Quality, and Source refer to the most reliable redshift for each object. If a redshift is available for an object from more than one source, then $\langle z \rangle$ gives the mean redshift from all sources, δz is the rms difference between them, and N_z is the number of redshifts included in the mean.

^aQuality codes: 0 = Quality unspecified by source, 1 = Secure, 2 = Probable, 3 = Uncertain

^bSource codes: 1 = Czoske et al. (2001), 2 = Frazier Owen (private communication), 3 = Hale/COSMIC, 4 = Keck/LRIS, 5 = Keck/DEIMOS

brighter than $I = 21.1$. At larger radii, and for dimmer E+S0s ($I < 22.5$), completeness drops to $\sim 50\%$. Spiral galaxies show a similar level of completeness, and so we reaffirm the conclusion of Paper I that there is no significant morphological bias in our redshift catalog (See Figure 3.) Our sample of E+S0 galaxies should be representative of the overall population, since the selection of galaxies for the spectroscopic survey was largely random, and the quality of the observed spectra depends only on random factors such as weather, introducing no bias with respect to spatial distribution.

3. ANALYSIS

The powerful combination of *HST* imaging and high-quality DEIMOS spectroscopy enables us to combine measures of the kinematic and photometric structure of cluster early types with detailed spectral information that reveals the underlying stellar population. Locally, early type galaxies show several tight correlations between kinematic, photometric, and spectral properties, such as the Fundamental Plane (FP) (Djorgovski & Davis 1987), the Mg- σ relation (Bender, Burstein, & Faber 1993), and the Balmer- σ relation (Kuntschner 2000; Kelson et al. 2001). Examining these relations at $z \sim 0.4$ not only gives insight into the redshift evolution of cluster early types, but, by examining the residuals from these relations as a function of cluster environment, we can uncover subtle trends in the mass to light ratios (M/L_V), metallicities, and star formation histories of these galaxies.

Of course, it is important first to clearly define meaningful measures of the cluster environment of a galaxy. Following Paper I, we measure radius as the distance from the center of the cluster's x-ray emission. Our results would be negligibly affected if we instead adopted the center of mass of the system determined by Kneib et al. (2003), as the two positions are separated by less than $5''$ (< 30 kpc). In order to more reliably study variations in galaxy properties as a function of local density, we re-calculate the local densities presented in Paper I, now making use of our extensive spectroscopic catalog, supplemented by the photometric redshift catalog of

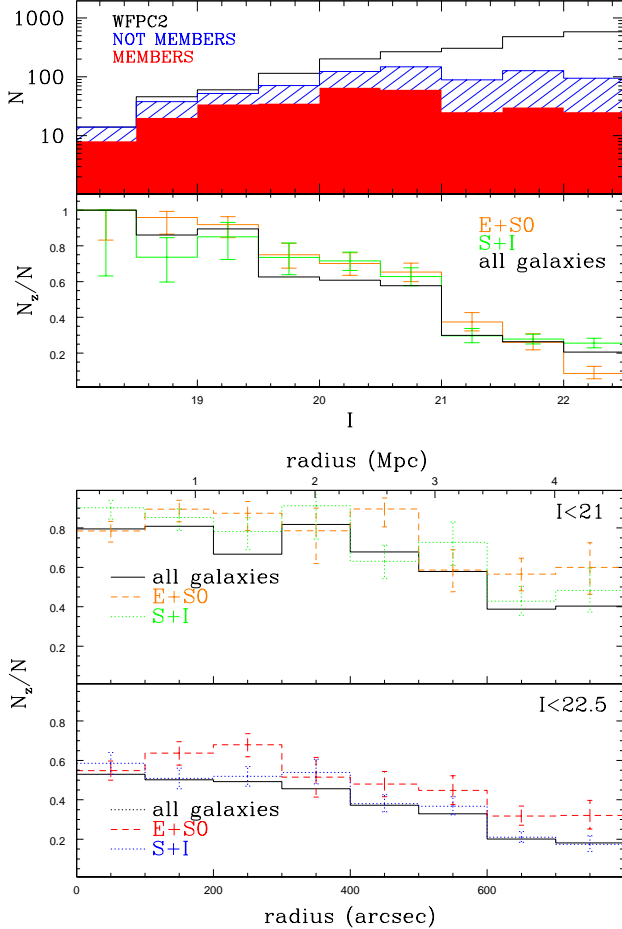


FIG. 3.— Top: Number counts as a function of I magnitude for all objects observed by WFCPC2, with the number of cluster members and nonmembers marked (upper panel). For all objects with WFCPC2 imaging, the lower panel displays the fraction with a measured redshift, as a function of I magnitude, and divided by morphology as indicated. Bottom: Fraction of objects with measured redshift, as in the top plot, but as a function of cluster radius, and to two separate magnitude limits, $I < 21.1$ (top) and $I < 22.5$ (bottom).

Smith et al. (2005).

Stellar velocity dispersions serve as a tracer of galaxy mass, and allow us to quantify how stellar populations vary with a galaxy's size (and, by extension, the formation history of the galaxy.) The redshift evolution of early type galaxies can be constrained by comparing the tight σ correlations observed locally to what is observed at higher redshift. We can also use velocity dispersions to determine if trends in stellar populations are more tightly correlated with environment or with galaxy mass.

With the addition of surface photometry from the *HST* images, we can derive the parameters of the fundamental plane (FP) in Cl 0024: effective radius R_e , mean surface brightness $\langle \mu_V \rangle$, and central velocity dispersion σ_0 (Djorgovski & Davis 1987; Dressler et al. 1987). The residuals from the FP reveal variations in the mass to light ratios of galaxies; from this, we can trace how the luminosity-weighted ages of early types vary across the cluster environment. We can also measure the evolution of M/L_V with redshift, and examine whether the amount of this evolution depends on galaxy mass and/or cluster environment.

We also wish to directly examine environmental trends in spectral line strengths, as these can reveal trends in current star formation (via [OII], [OIII], or $H\beta$ emission), recently completed star formation (via $H\gamma$ and $H\delta$ absorption line strengths), or metallicity (via Mg_2 , Mg^b or the composite index $[MgFe]'$).

Below, we discuss the methods we follow to accurately measure each of the quantities necessary for our analysis: local density, velocity dispersion, surface photometry, and spectral line indices.

3.1. Local Density Measurements

Local density measurements in Paper I relied on a statistical field subtraction, following the methods of previous work (e.g. Whitmore et al. 1993; Dressler et al. 1997). While adequate, we can improve on these measurements by making use of our large spectroscopic catalog, supplemented by the extensive catalog of photometric redshifts from Smith et al. (2005). These catalogs allow us to eliminate most foreground and background galaxies, and calculate local densities based only on the positions of confirmed or possible cluster members. A standard method of measuring local density, used in Paper I and first introduced by Dressler (1980), involves calculating the area enclosed by the ten nearest neighbors of a galaxy (to $I = 21.1$ in the case of Paper I). In order to obtain local density measurements for our entire sample of 104 galaxies ($I \leq 22.5$), we modify the method from Paper I to include all fainter galaxies to $I = 22.5$ in the tally of nearest neighbors. Our method is as follows:

Each object with $I < 22.5$ is given a weight between zero and one, according to the procedure outlined below. Then, for each object, we calculate the total area enclosed by a set of neighboring galaxies whose cumulative weight equals about 10. (Fractional weights are common, so the total weight rarely equals exactly 10.) The local density is then calculated by dividing the total weight by the area in Mpc^2 . Compared to the method used in Paper I, this should give a value of Σ_{10} that is a better reflection of the true density of galaxies in the cluster, minimizing errors due to chance superpositions of background galaxies or groups.

As we wish to include only cluster members in the calculations of local density, we assign weights to galaxies based on how confident we are that it is a cluster member. If a spectroscopic redshift is available from the combined catalog (§ 2.2.2), then the object's weight equals 1 if it is a cluster member ($0.374 < z < 0.402$), and zero otherwise.

For objects with no spectroscopic redshift, we check for a photometric redshift in the catalog of Smith et al. (2005). While the cluster is clearly evident in the redshift distribution of galaxies in the Smith et al. (2005) catalog, the limited accuracy of photometric redshifts means that the cluster galaxies are smeared across the redshift range $z_{phot} = 0.39 \pm 0.09$. We give all galaxies within this range a weight of 1, even though some non-cluster members will be mistakenly included. From an analysis of galaxies with both spectroscopic and photometric redshifts available, we find that approximately 85% of cluster members have photometric redshifts in the adopted range, and about one third of all galaxies with photometric redshifts in this range will actually lie outside of the cluster. This will lead us to slightly overestimate the total number of cluster members, and, by extension, local densities. But the effect is minimal given the large fraction of spectroscopic redshifts. We also explored a more elaborate weighting scheme based on the joint probability that a given galaxy will be a

member according to its photometric redshift and projected radius. The rms variation in Σ_{10} between this and our simple scheme is about 12% - less than other sources of uncertainty and therefore not worthy of adopting.

The photometric redshift catalog is J-limited at $J \leq 21.5$, so there are some objects with $I < 22.5$ that have neither a spectroscopic nor photometric redshift available. For these, we assign weights according to the radial dependence of the probability that a random galaxy will be a cluster member. For example, based on the combined spectroscopic redshift catalog, the probability is 81% that an unknown galaxy within 0.75 Mpc of the cluster core is a cluster member; such a galaxy is assigned a weight of 0.81. We calculate and assign similar probabilities for galaxies in several different radial bins out to 5 Mpc. Since we only consider galaxies within the magnitude range $17.75 \leq I < 22.5$, the probabilities we have adopted do not vary strongly with magnitude, and so we do not further subdivide our probability estimates into different bins for different ranges of galaxy magnitude.

In order to properly compare densities calculated with our method to those used in Paper I, we also calculate Σ_{10} using objects brighter than $I = 21.1$. A tight correlation is seen between the two estimates which agree to within 20%; we also reproduce the overdensities at ~ 1 Mpc and ~ 3 Mpc given in Paper I. Similarly, we can compare the density of background objects predicted by our method to the field number counts of, e.g., Abraham et al. (1996a) and Postman et al. (1998). We calculate background count densities of $\log(N)/\text{deg}^2 = 4.45 \pm 0.05$ (to $I = 22.5$) and 3.90 ± 0.07 (to $I = 21.1$). Our predicted counts agree with both Abraham et al. (1996a) and Postman et al. (1998), within the uncertainties, for both magnitude limits. As an additional check on the uncertainty in Σ_{10} measured to our deeper limit ($I = 22.5$), we calculated a density (Σ_5) for a total weight of 5. The rms variation between Σ_5 and Σ_{10} is about 25%. Conservatively, we adopt this as the uncertainty in Σ_{10} .

3.2. Stellar Velocity Dispersions

We are able to measure velocity dispersions only for our brighter sample of early-type members ($I < 21.1$), as our spectra of fainter galaxies do not have sufficiently high signal to noise. In order to determine velocity dispersions, we fit to a grid of stellar templates degraded to the instrumental resolution and smoothed to various velocity dispersions (van der Marel 1994). A high quality spectrum for an object near our magnitude limit is plotted in Figure 1, with the best-fitting template spectrum overplotted.

To determine the signal/noise limit at which our velocity dispersion measures become unreliable, we performed a series of Montecarlo simulations. We construct fake galaxy spectra from stellar templates smoothed to the resolution and pixel scale of DEIMOS (for the 900 line/mm grating), truncated to an identical length of $\sim 2600\text{\AA}$, convolved with a Gaussian of various widths to simulate different velocity dispersions, and degraded to a variety of signal to noise ratios. We then attempt to recover the velocity dispersion of the fake galaxy by running the same code as above.

We find that the approximate mean S/N where systematic errors in σ reach $\sim 10\%$ corresponds to $S/N = 7 - 8$ (\AA^{-1} , observer's frame). Below this level, velocity dispersion measures rapidly become inaccurate. In our high quality sample, we include galaxies with S/N near this limit, though most have $S/N > 10$. However, we place a somewhat

stricter limit ($S/N > 8$) on the spectra observed with LRIS and the DEIMOS 600 lines/mm grating which have slightly worse spectral resolution. Only 10 high quality spectra have $S/N < 10$, so our results are fairly insensitive to these choices. Table 3 lists all galaxies with high quality spectra, along with their velocity dispersions, formal errors, and the mean signal/noise of the spectrum.

The typical uncertainty in our velocity dispersion measurements is $\pm 10\%$. These errors are dominated by differences in σ that depend on the template spectrum used, though systematic errors rise to become equally important as we approach the signal to noise limit. Of the early-types where we measured velocity dispersions, there were three galaxies in common with an earlier study of Cl 0024 by van Dokkum & Franx (1996); the velocity dispersions quoted in van Dokkum & Franx (1996) match ours in all three cases, with $< \delta\sigma/\sigma > = -0.02 \pm 0.13$. Treu et al. (2005b) derived stellar velocity dispersions from DEIMOS spectra using a similar method to our own. They pursued several tests to determine the accuracy of their dispersions, and found an rms uncertainty of $\sim 12\%$, in agreement with our own uncertainty estimates. For more discussion of such accuracy tests, see Treu et al. (2005b).

For each galaxy, we apply a correction to match the central velocity dispersion measured through a $3.4''$ aperture at the distance of Coma, following the prescription of Jørgensen, Franx, & Kjærgaard (1995a). This choice of aperture size for the correction is somewhat arbitrary, but is a common choice for studies of early-type galaxies at low to intermediate redshift (e.g. Kelson et al. 2000b; Wuyts et al. 2004) because it facilitates comparison to local measurements of the Fundamental Plane (e.g. Jørgensen, Franx, & Kjærgaard 1996). The magnitude of this correction depends on the physical scale over which the 1D spectrum was extracted, which varies from object to object. The average correction applied is $6.6\% \pm 0.4\%$. Corrected velocity dispersions are denoted by σ_0 , and are listed in Table 3.

3.3. Surface Photometry

GALFIT (Peng et al. 2002) was used to derive effective radii and surface brightnesses for all galaxies with measured velocity dispersions. For each galaxy, we extract postage stamps approximately 200 pixels on a side ($\sim 10''$). We then use *GALFIT* to fit against a model de Vaucouleurs ($r^{1/4}$) profile. Following other authors, e.g. Jørgensen, Franx, & Kjærgaard (1995b), we fit all E+S0s to the same profile shape, even though some may be better described by a lower Sérsic index, or a de Vaucouleurs plus exponential function. (See Peng et al. (2002) for a definition of the Sérsic function, a more general form of the de Vaucouleurs function.)

GALFIT minimizes the χ^2 residuals between the galaxy image and a 2D galaxy model that it constructs. The free parameters in this model profile include: R_e , total magnitude, axis ratio, galaxy position angle, the position of the galaxy center, and the sky level. Sky levels were set according to the header of each WFPC2 image, but were allowed to vary within a small range to ensure that *GALFIT* converges to the correct fit.

Model galaxies are convolved with a PSF before fitting; we use a star observed on the same WFPC2 chip, with approximately the same exposure time. We tested with a number of different stars, and found that the specific choice of PSF star did not significantly affect the derived photometric param-

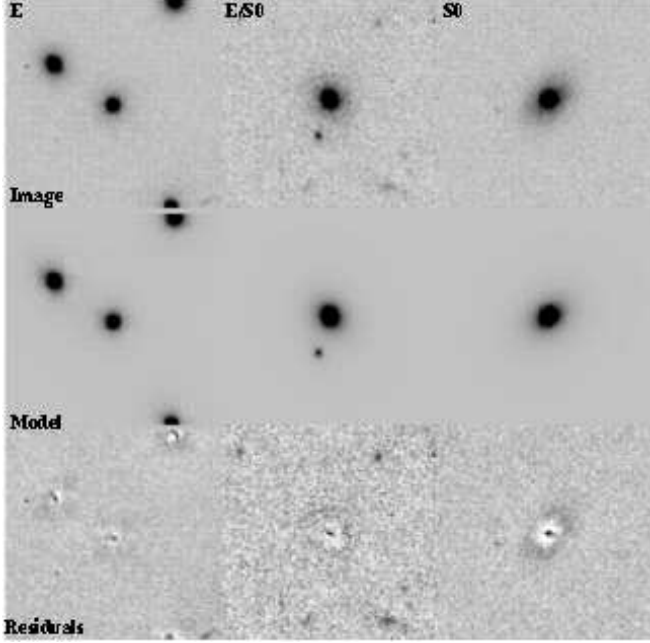


FIG. 4.— Example surface photometry fits, for galaxies classified as E, E/S0, and S0 by Paper I. Top row is the galaxy image. Middle row shows the GALFIT model image. Bottom row shows the residuals of the image fit to model.

ters.

When fitting a galaxy to a de Vaucouleurs profile, the best-fit parameters are particularly sensitive to extra flux far from the galaxy's center (Peng et al. 2002), since the function declines relatively slowly beyond R_e . Neighboring or overlapping galaxies thus contribute light that must be either masked or removed by fitting multiple galaxy profiles. To best remove this extra light, we simultaneously fit a Sérsic profile to each bright neighbor within the postage stamp image. The Sérsic function is the best choice for such a fit because its form is general enough to successfully model a wide range of galaxy types; according to Peng et al. (2002) this ensures that the galaxy's flux is subtracted uniformly.

The magnitude of the best-fit model galaxy returned by *GALFIT* is measured in the observed F814W filter. At $z \sim 0.4$, this is a close match to rest-frame V, but we must still apply a small *k*-color correction to derive the mean surface brightness in rest frame V. $\langle \mu_V \rangle$ is defined as:

$$\begin{aligned} \langle \mu_V \rangle &= I_{814W} + 2.5 \log(2\pi R_e^2) + \Delta m_{VI} - A_I - 10 \log(1+z) \\ &= I_{814W} + 5 \log(R_e) + 1.29 \pm 0.04 \end{aligned}$$

where $A_I = 1.95E(B-V)$ (Schlegel et al. 1998) corrects for galactic extinction, the redshift term accounts for cosmological dimming, and Δm_{VI} is the *k*-color correction. In the second line of the above equation, we insert our adopted values: $\Delta m_{VI} = 0.85 \pm 0.03$, adopted from calculations by Treu et al. (2001a), $A_I = 0.11 \pm 0.01$ from Schlegel et al. (1998), and $z \sim 0.395$.

Since we only measure surface photometry for our brighter sample of galaxies ($I < 21.1$), formal statistical errors in the measured parameters are very small: less than $0.05''$ in R_e , and 0.05 in magnitude. We estimate that systematic errors are double these values, and adopt $0.1''$ and 0.1 mag as typical errors in R_e and magnitude, respectively. There may be

additional uncertainty in R_e and μ_V related to the choice of a de Vaucouleurs profile over other structural forms, but previous work (Fritz et al. 2005; Kelson et al. 2000a; Saglia et al. 1993) has shown that the combination of R_e and μ_V that enters into the Fundamental Plane (see § 4) is largely insensitive to the galaxy profile adopted. Figure 4 shows three example fits, for galaxies classified as E, E/S0, and S0. For each galaxy, we display the original galaxy image, the best-fit model image, and the residuals. As might be expected, the residuals are smaller for the fit to the elliptical galaxy; the residuals for the S0 galaxy clearly show a disk component that is not well fit by a de Vaucouleurs profile.

We observed two clear edge-on S0s which had to be removed from our sample of high-quality spectra, due to the uncertainty in trying to fit a de Vaucouleurs profile to such an edge-on disk. We also removed two galaxies with bad fits, defined as where the SExtractor magnitude from the *HST* image and *GALFIT* model magnitude differ by more than 0.75—the two magnitudes for most galaxies in our sample match to much better than 0.75 magnitudes. None of these four galaxies are included in the previously defined sample of 71 high-quality early-types, though they are included in the larger sample of 104 galaxies. The photometric parameters for the high-quality galaxies are listed in Table 3.

As a check on our measurements, we compared our R_e and $\langle \mu_V \rangle$ for three galaxies that also were studied in the work by van Dokkum & Franx (1996). (This is not the same set of three we used to compare velocity dispersions in § 3.2: for one galaxy where each group has measured surface photometry, we have not measured σ . And for one galaxy where we have both measured σ , we do not have an *HST* image for surface photometry.) In each case, our surface photometry matches theirs, within the adopted errors on our measurements. We exclude one additional galaxy that we have in common with van Dokkum & Franx (1996), as it exhibits a disturbed morphology (the triple nucleus galaxy discussed in their paper.)

3.4. Line Strength Measures

We measure the strengths of several diagnostic spectral lines for the entire sample of early-type galaxies (to $I < 22.5$). In order to best probe the stellar population of each galaxy, we select a set of indices that are sensitive to a range of star formation histories and metallicities. Emission lines, such as [OII], [OIII], and sometimes H β indicate ongoing star formation (or possibly nuclear activity). Balmer absorption lines, such as H γ and H δ are sensitive to recently completed star formation; these lines are strongest in A-stars, which contribute prominently to a galaxy's integrated starlight within the first Gyr after a burst of star formation. We also measure several metallicity indicators, such as Mg $_2$, Mg $_b$, Fe5270, Fe5335, and the composite index $[MgFe]'$, which is defined as:

$$[MgFe]' \equiv \sqrt{Mg^b(0.72 * Fe5270 + 0.28 * Fe5335)}$$

In the local universe, $[MgFe]'$ seems to be insensitive to variations in α -element abundance (Thomas et al. 2003), making it a valuable tracer of total metallicity.

Where possible, we adopt the Lick index definitions to measure the strength of each spectral line (Worthey et al. 1994). In the Lick system, the equivalent width of a line is measured by defining a wavelength range to either side of a main index bandpass. The mean level of each sideband is determined,

and a straight line is fit, defining the “pseudo-continuum” across the index bandpass. The equivalent width of the line within the index bandpass is then measured with respect to the pseudo-continuum level. The Lick system does not include an index for [OII], so we adopt the one defined by Fisher et al. (1998). In Figure 1 we plot an example spectrum with the wavelength ranges of several indices and their sidebands marked. For clarity, the results in § 4 will concentrate primarily on three representative sets of measurements: [OII], $(H\gamma_A + H\delta_A)$, and $[MgFe]'$.

Table 3 lists the strengths of several key spectral lines, for all 104 galaxies in our sample. These raw indices are suitable for examining environmental trends within our own data set, but in order to make a proper comparison to other published data or theoretical models, we must carefully correct for any systematic differences between each set of measurements. In particular, index strengths are known to vary with the spectral resolution of the data. While we attempt to compare our data only to measurements made at high spectral resolution, to take full advantage of the high resolution available with DEIMOS, in some cases we are forced to degrade the resolution of our spectra to match that of the comparison data or model.

In § 4 and § 5, we will compare some of our results to the stellar population models of Bruzual & Charlot (2003), which include full synthetic spectra at a resolution of 3Å; this is the closest match available to the intrinsic resolution of our DEIMOS spectra ($\sim 1\text{\AA}$). We will also examine the Balmer– σ relation in comparison to data measured at 10Å resolution (Kelson et al. 2001), the approximate resolution of the original Lick system (Worley et al. 1994). Therefore, we convolved our DEIMOS spectra with Gaussians to produce degraded spectra at both 3Å and 10Å resolutions. We then re-measured the relevant spectral line indices. While not included in Table 3, spectral index measurements from our degraded DEIMOS spectra are available from the authors by request.

To compare our Balmer– σ relation to previous work by Kelson et al. (2001) on the redshift evolution of this correlation, we apply an aperture correction to our $H\delta_A$ and $H\gamma_A$ line strengths; we adopt their estimate that the quantity $(H\delta_A + H\gamma_A)$ varies with aperture as:

$$\Delta(H\delta_A + H\gamma_A) = 1.78 \pm 0.16 \Delta \log(D_{ap})$$

and correct to an aperture of 1''.23 at $z = 0.33$. This is a very small correction to our data, which was measured through a similar aperture size at slightly higher redshift.

For any fixed-width absorption line index, Doppler broadening of lines will cause measured equivalent widths to be underestimated: as velocity dispersion increases, more of the line’s flux falls outside of the index bandpass. We can correct for this effect by modeling how each index varies with σ , with the help of the Bruzual & Charlot (2003) population synthesis models. We select several of their theoretical spectra at 3Å resolution and zero velocity dispersion, and broaden them to a series of different velocity dispersions. At each σ , we measure the line indices we wish to correct: $[MgFe]'$, $H\delta_A$, and $H\gamma_A$. We then fit a quadratic function in σ to the resulting set of measurements. We find that the σ correction depends on the initial resolution of the spectrum, so we also degrade the Bruzual & Charlot (2003) spectra to 10Å resolution, and repeat the procedure to determine the proper correction for our low-resolution measures of $H\delta_A$ and $H\gamma_A$.

Since we are not able to measure velocity dispersions for our full sample of 104 galaxies, corrected indices only appear in plots that are limited to the 71 bright galaxies where we have accurate measurements of σ . All plots that demonstrate trends in the full sample of 104 E+S0s are shown with uncorrected indices only. However, not applying a σ correction in these cases produces only a small error: less than $\pm 0.8\text{\AA}$ in $(H\delta_A + H\gamma_A)$. Emission lines like [OII] do not vary regularly with σ , as the source of emission is generally not spread evenly across a galaxy.

In order to compare observed spectral line strengths to the predictions of Bruzual & Charlot models with various star formation histories, we need to calibrate our observed [OII] equivalent widths to specific star formation rates ($M_\odot/M_{gal} \text{ yr}^{-1}$). We make such a calibration using the deep H α imaging of Cl 0024 by Kodama et al. (2004, and private communication). First, equivalent widths from the two catalogs are cross-correlated: our [OII] widths closely track those in H α , approximately reproducing the locally-observed trend (Kennicutt 1992). For each H α detection, Kodama also provide an estimated star formation rate, which we convert to a specific star formation rate by dividing by an estimated mass for each member. For galaxies with velocity dispersions available, we calculate a galaxy’s dynamical mass according to $M = 5\sigma^2 R_E/G$. To estimate a stellar mass for a galaxy with no available velocity dispersion, we first determine the typical M/L_V for a local galaxy of this luminosity from Gerhard et al. (2001), and correct M/L_B to M/L_V by subtracting a factor equal to $\log(M/L_V) - \log(M/L_B) = -0.06$, estimated from the typical colors of nearby early type galaxies. We then correct for redshift evolution in M/L_V (based on our Fundamental Plane results below), and multiply by the observed luminosity of the galaxy:

$$\log(M) \simeq \log(M/L_V) + <\Delta \log(M/L_V)> + \log(L_V)$$

For galaxies with velocity dispersions, masses estimated in this way are consistent with the calculated dynamical masses ($\Delta \log(M/M_\odot) = \pm 0.3$). We then fit a straight line to measured [OII] versus specific star formation rate ($M_\odot/M_{gal} \text{ yr}^{-1}$), to yield a conversion relationship between the two.

In order to visualize overall trends in the spectral properties of cluster early types, we also produce a series of co-added spectra for each radial zone. Each spectrum is normalized, shifted to the rest frame, and then co-added. Bad pixels and sky lines are given zero weight in the addition. This method provides a snapshot of what the average spectrum of each ensemble of galaxies looks like. While weighting by luminosity would better represent the integrated stellar population of each ensemble, in practice, the co-added spectrum is dominated by the brightest galaxy in each group. We must be careful, however, in interpreting differences between the coadded normalized spectra for each radial zone: each coadded spectrum will reflect an ensemble of galaxies with a different average size and magnitude. Therefore, it is difficult to separate radial trends in the spectra from trends with magnitude or size. These co-added spectra will be discussed below in conjunction with the environmental trends in the spectral indices of individual galaxies.

4. RESULTS

4.1. Cluster: Empirical Scaling Laws

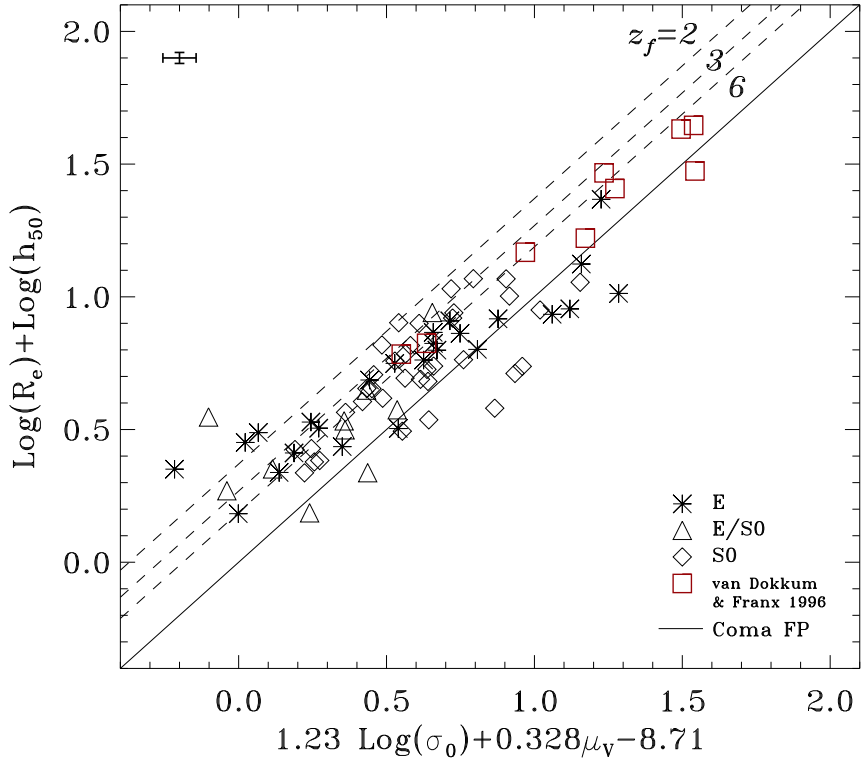


FIG. 5.— FP of Cl 0024, compared to Coma cluster (solid line). Symbols represent different morphologies, as indicated. Dotted lines correspond to the expected shift in FP zero point from Coma to $z \sim 0.4$, for SSP models with $z_f = 2.0, 3.0, 6.0$.

Before we examine environmental trends in galaxy properties, we present the overall Fundamental Plane, $[\text{MgFe}]' - \sigma$ relation and the Balmer– σ relation for the cluster sample with high quality spectra, and discuss how each has evolved between $z \sim 0.4$ and the present epoch.

4.1.1. The Fundamental Plane

Previous studies have traced a mild shift in the intercept of the cluster FP with redshift (Fritz et al. 2005; Wuyts et al. 2004; Kelson et al. 2000b). This seems to be consistent with passive luminosity evolution of stellar populations with a high redshift of formation (Wuyts et al. 2004), though biases due to morphological evolution are difficult to quantify. However, most earlier studies have concentrated on measuring the evolution of the FP from data taken in intermediate or high redshift cluster cores. With our broader spatial coverage, we can uncover any significant difference in the mean M/L_V of early types as a function of radius. Our sample also extends to fainter magnitudes than previous studies at $z \sim 0.4$, allowing us to probe M/L_V for smaller early-types that perhaps formed later than the most massive cluster ellipticals.

Figure 5 presents the FP of Cl 0024 compared to that of the Coma cluster, adopting the parameters determined locally by Lucey et al. (1991): $\alpha = 1.23$, $\beta = 0.328$, and $\gamma = -8.71$, where the fundamental plane is defined as

$$\text{Log}(R_e) = \alpha \text{Log}(\sigma_0) + \beta \langle \mu_V \rangle + \gamma$$

If we assume for the moment that α and β remain fixed with

redshift—i.e., that E+S0s evolve passively—then we can relate the offset in the intercept γ between CL 0024 and Coma to the change in the mean mass to light ratio of cluster early types since $z = 0.4$:

$$\langle \Delta \log(M/L_V) \rangle = \langle \Delta \gamma \rangle / (2.5\beta)$$

We find that the average offset from the Coma FP implies a change in the M/L_V ratio between $z = 0.4$ and $z = 0.02$ of $\langle \Delta \log(M/L_V) \rangle = -0.14 \pm 0.02$, excluding galaxies with velocity dispersions below 100 km s^{-1} . (Including those galaxies, the zero point shift rises to $\langle \Delta \log(M/L_V) \rangle = -0.18 \pm 0.03$) This is a smaller evolution than found in the field at $z \sim 0.3 - 0.5$ by Treu et al. (2005b), $\langle \Delta \log(M/L_V) \rangle = -0.23 \pm 0.05$, though it is in agreement with the offset determined by Kelson et al. (2000b) for a cluster at $z = 0.33$ ($\langle \Delta \log(M/L_V) \rangle = -0.17 \pm 0.03$). Overplotted in Figure 5 are dotted lines representing the expected evolution of the FP zero point from the Coma cluster back to $z = 0.4$. These are based on the passive evolution of Single Stellar Population (SSP) galaxy models, with a redshift of formation, z_f , of 2, 3, or 6 (Bruzual & Charlot 2003). The observed FP in Cl 0024 is consistent with $z_f > 3$ for most cluster early types.

Open squares in Figure 5 indicate points from van Dokkum & Franx (1996), who also measured the FP in Cl 0024. The two sets of data fall on the same plane, and our inferred $\langle \Delta \log(M/L_V) \rangle$ is consistent with their work: they calculated $\langle \Delta \log(M/L_V) \rangle = -0.12 \pm 0.03$. Our much larger sample should allow for greater precision in

TABLE 4
 $\langle \Delta \log(M/L_V) \rangle$ FOR SEVERAL SUBSETS OF OUR DATA.

	E	E/S0	S0	All	All+vDF
All σ:					
N:	24	10	35	69	77
$\langle \Delta \log(M/L_V) \rangle$:	-0.18 ± 0.05	-0.23 ± 0.08	-0.14 ± 0.03	-0.18 ± 0.03	-0.18 ± 0.02
$\pm 1\sigma$:	0.23	0.26	0.20	0.20	0.19
$\sigma > 100 \text{ km s}^{-1}$:					
N:	21	8	33	62	70
$\langle \Delta \log(M/L_V) \rangle$:	-0.14 ± 0.03	-0.14 ± 0.06	-0.14 ± 0.03	-0.14 ± 0.02	-0.14 ± 0.02
$\pm 1\sigma$:	0.15	0.17	0.18	0.16	0.16
$R < 1 \text{ Mpc}, \sigma > 100 \text{ km s}^{-1}$:					
N:	10	6	15	31	39
$\langle \Delta \log(M/L_V) \rangle$:	-0.09 ± 0.06	-0.10 ± 0.06	-0.06 ± 0.06	-0.07 ± 0.03	-0.09 ± 0.03
$\pm 1\sigma$:	0.18	0.16	0.22	0.20	0.19

NOTE. — The first three columns present the mean evolution in M/L_V broken down by morphological type, both with and without galaxies of $\sigma < 100 \text{ km s}^{-1}$, and for the whole cluster sample or just galaxies with projected radius $R < 1 \text{ Mpc}$. Column four includes all our E+S0s, but excludes two disturbed-morphology galaxies with outlying values of $\Delta \log(M/L_V)$. In the fifth column, we add our data to the eight galaxies from van Dokkum & Franx (1996) that do not overlap with our own. $\pm 1\sigma$ values are logarithmic, representing the scatter in $\Delta \log(M/L_V)$.

calculation of the FP zero point, yet the two measurements yield similar uncertainties in $\langle \Delta \log(M/L_V) \rangle$. This is due to the surprisingly high scatter that we uncover in the Cl 0024 FP, which was not apparent in the earlier sample of 9 galaxies in van Dokkum & Franx (1996).

Importantly, we find the intrinsic scatter in the FP of Cl 0024 is 40% in M/L_V , significantly higher than the $\sim 20\%$ found locally (e.g. Jørgensen, Franx, & Kjærgaard 1996), and also higher than the $\sim 13\%$ scatter in the FP of Cl 1358+62 at $z = 0.33$ (Kelson et al. 2000b). While we probe the FP for a larger range of galaxy masses than Kelson et al. (2000b), we see a higher scatter even in the more massive galaxies that are comparable to those in their study. Interestingly, this increased scatter is due almost entirely to an enhanced scatter in M/L_V for galaxies within the inner 1 Mpc of the cluster, a region that has been well studied in other clusters in this redshift range (Bender et al. 1998; Kelson et al. 2000b; Ziegler et al. 2001). To verify this increased scatter is a true physical effect, we examined the possibility that errors in our surface photometry are higher in the more crowded cluster core, but found that galaxies with nearby neighbors cannot account for the high scatter. We also checked for errors in our velocity dispersion measurements: when removing five early type spectra ($\sigma > 100 \text{ km s}^{-1}$) with $S/N < 10$ from our high quality sample, we find no significant change in our FP zero point or scatter.

A similarly large scatter was found by Wuyts et al. (2004) for the cluster MS 2053-04 at $z = 0.58$ ($\sim 42\%$), so this may be an effect seen only in some fraction of intermediate redshift clusters. At even higher redshift, Holden et al. (2005) finds a large scatter in M/L_B for massive early types at $< z > = 1.25$. We will defer further discussion of this effect to § 4.2, where we discuss radial trends.

Recent results indicate that the parameters of the FP at intermediate redshift may differ from the local values (e.g. Treu et al. 2005a,b, Wuyts et al. 2004; van der Wel et al. 2005). We investigated using the method of Jørgensen, Franx, & Kjærgaard (1996) to derive an inde-

pendent fit for the parameters of the FP from our sample, including Montecarlo simulations to account for bias in our magnitude-limited sample, but found no conclusive evidence for a change in FP parameters from the local values.

Nevertheless, the group of galaxies with $\sigma < 100 \text{ km s}^{-1}$ in Figure 5, located at the lower left of the plot, seem to deviate significantly from the FP. As most calculations of the FP parameters specifically exclude galaxies with $\sigma < 100 \text{ km s}^{-1}$ (e.g. Jørgensen, Franx, & Kjærgaard 1996; Lucey et al. 1991), including our own, it is not surprising that such galaxies in our sample deviate from the FP. Yet there is also evidence that, in the local universe, these small ellipticals and dwarf ellipticals may behave differently as a population than larger E+S0s (e.g. Burstein et al. 1984). Our data suggest that this population split may have existed already at $z \sim 0.4$. When dividing our sample into three subclasses (E, S0, and E/S0), we find no evidence of significant variation between the populations, either in scatter or intercept. Table 4 lists values of $\langle \Delta \log(M/L_V) \rangle$ and the scatter about the mean for several different subsamples of our data. For galaxies with $\sigma > 100 \text{ km s}^{-1}$ in particular, there appears to be no variation at all between E, E/S0, and S0 morphological types. This lack of variation is in disagreement with recent results by Fritz et al. (2005), who marginally detect a difference between ellipticals and S0s in two clusters at $z \sim 0.2$, equivalent to a difference in $\delta \langle \log(M/L_V) \rangle$ of $\sim -0.16 \pm 0.11$ (with S0s being the younger/more luminous population). On the other hand, Kelson et al. (2001) find no such distinction between ellipticals and S0s at $z = 0.33$. Our sample is larger than either of these other studies, and so we place stronger constraints on the possible M/L_V variations between Es and S0s at $z \sim 0.4$. As discussed in §2, we attempted to improve our E:S0 classification by examining residuals from our surface photometry fits as a means of locating faint disks or bars (See Figure 4). Two of us (RSE and TT) independently examined the residuals and, although the revised classes agreed fairly closely, no significant FP differences between ellipticals and S0s were found.

4.1.2. $[MgFe]'$ – σ and Balmer– σ relations

While the FP helps to connect the dynamic and photometric structure of an early type galaxy to the overall mass to light ratio of its stellar population, we can seek an improved picture of a galaxy's stellar population by also examining correlations between spectral line strengths and σ . Local early type galaxies exhibit a tight correlation between the Mg_2 line index and σ , for example (e.g. Kuntschner et al. 2001). The narrower Mg^b index is centered over the same spectral feature, and, at least locally, behaves in the same way as Mg_2 (Burstein et al. 1984). Similarly, correlations are observed between σ and the strengths of several Balmer lines: $H\beta$, $H\gamma$ and $H\delta$ (Kelson et al. 2001; Kuntschner et al. 2001).

Our current set of high quality spectra of early types in Cl 0024 provides a large sample of galaxies at $z \sim 0.4$ where diagnostic spectral lines can be measured with some accuracy for the first time. We measure Mg^b , Mg_2 and the composite index $[MgFe]'$ to make a broad comparison between the metallicity features of early types at intermediate redshift and those seen locally.

We also measure Balmer line strengths, which are commonly used to judge the age of early type galaxies (Worthey & Ottaviani 1997). However, low levels of recent star formation can make an early-type galaxy's stellar population appear much younger than the true average age of its stars. For the first 1 Gyr after a starburst, the strong Balmer absorption present in the spectra of A stars can be prominent in the integrated galaxy spectrum. The $H\beta$ index is a particularly age-sensitive indicator, but is affected by contamination from emission. While $H\alpha$ can be used to correct $H\beta$ for small amounts of emission, this line falls outside of the range of our spectra, so we choose to study the $H\delta$ and $H\gamma$ lines instead, which are relatively unaffected by emission. Measuring $H\delta$ and $H\gamma$ in Cl 0024 can thus allow us to probe both galaxy age and episodes of recent star formation, if the two effects can be separated.

Early attempts to trace the evolution of these relations with redshift has produced a variety of results. Kelson et al. (2001) reported a correlation between $(H\delta+H\gamma)$ and σ for several clusters between redshifts of 0.08 and 0.83. The slope they measure for Cl 1358+62 at $z = 0.33$ is consistent with their data at all other redshifts, though they are unable to measure slope for each cluster individually. They plot the zero point evolution of this relation, and find that the change in mean Balmer absorption strength from $z = 0.83$ to the present epoch is consistent with passive evolution models of early types, and constrain $z_f > 2.4$. Likewise, Barr et al. (2005) study a poor cluster at $z = 0.28$ and find that the zero point evolution of the $(H\delta+H\gamma)$ – σ relation, when compared to Kelson et al. (2001), is only marginally inconsistent with passive evolution.

Conversely, the evolution of the metallicity correlations has proven more complicated. The question of using spectral line strengths to uniquely determine ages, metallicities, and α -element enhancement ratios for elliptical galaxies is not yet solved even for local galaxies, as made clear by the excellent study of the problem by Tantalo & Chiosi (2004). Further, our data likely fall short of the S/N needed to determine these galaxy properties reliably (Trager et al. 1998). It is therefore beyond the scope of this paper to examine how the various Mg – σ , $[MgFe]'$ – σ and Balmer– σ relations evolve with redshift.

However, we note that correlations with velocity dispersion do exist as far back as $z \sim 0.4$, regardless of the origin of

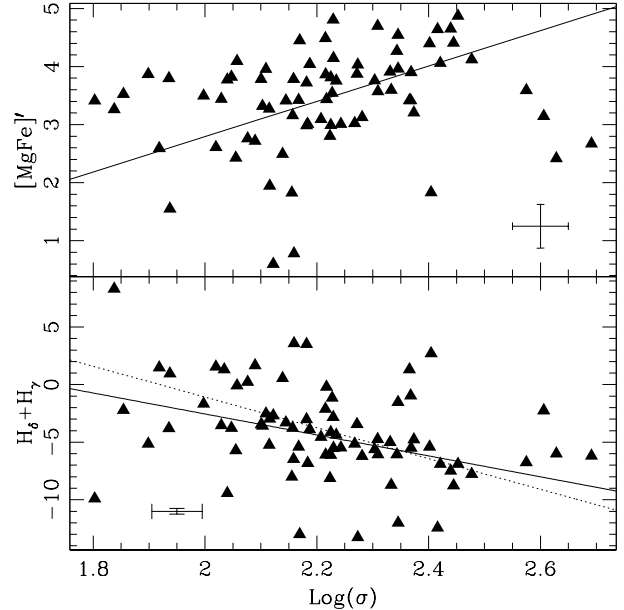


FIG. 6.— Top: $[MgFe]'$ – σ at resolution of 3 Å. The solid line is the best least-squares fit to our data, excluding the outlier points at $\sigma \geq 300$ km s $^{-1}$. Bottom: $(H\delta+H\gamma)$ – σ at resolution of ~ 10 Å, compared to Kelson et al. (2001), at same spectral resolution. Indices are corrected to match the aperture used by Kelson et al. The solid line represents the best-fit relation from Kelson et al. (2001). We adopt the slope of their relation, but calculate the intercept at $z = 0.4$ by interpolating between their data points at $z = 0.33$ and $z = 0.58$. The dashed line is the line of best fit to our data. The scatter is large, so our best-fit relation is highly uncertain. In both panels, velocity dispersions are aperture corrected to a 3.4'' diameter aperture at the distance of the Coma cluster.

such a relation. Secondly, large deviations from these relations may indicate a recent episode of star formation in that galaxy. It will be useful then to look later at the residuals from the $[MgFe]'$ and Balmer– σ relations, as a function of cluster environment.

We can minimize uncertainties due to variations in abundance ratio by focusing on the $[MgFe]'$ index, which should provide a reliable estimate of the total metallicity of a galaxy (Thomas et al. 2003). Figure 6 presents the correlation between $[MgFe]'$ and σ . The bulk of galaxies measured fall along the solid best-fit line plotted, though the scatter is high. The high scatter could be due to the large error bars on each measurement. However, there are a significant number of outliers with anomalously low $[MgFe]'$ that seem not to be due to measurement errors. These outliers correlate with other properties of the each galaxy's stellar population, and will be discussed further in § 5.

Figure 6 presents $(H\delta+H\gamma)$ vs. σ for Cl 0024. The two quantities correlate in the sense that the largest, highest σ galaxies exhibit the weakest Balmer absorption. This is as expected if the stellar populations are oldest in the largest elliptical galaxies. Overplotted in Figure 6 is the best-fit relation from Kelson et al. (2001), where we adopt their slope and interpolate between their points at $z = 0.33$ and $z = 0.58$ to determine the zero point at $z = 0.39$. Our data is consistent with their findings, though again our scatter is quite large. We also overplot our best fit relation as a dotted line, though the high scatter makes this relation highly uncertain.

In fact, just as we saw with the FP of Cl 0024, we see a

scatter that is much larger than that observed in Cl 1358+62 at similar redshift. Both the FP and $(H\delta+H\gamma)-\sigma$ relation are reported to be much tighter for Cl 1358+62 than for Cl 0024 (Kelson et al. 2001, 2000b). On the other hand, Barr et al. (2005) also find an increased scatter in the $(H\delta+H\gamma)-\sigma$ relation at $z = 0.28$, though they do not measure the FP. As with the FP and Metallicity- σ relation in Cl 0024, some of the enhanced scatter we observe in Balmer line strengths is a direct signature of environmental evolution, and will be discussed in § 4.2.3 below.

4.2. Radial Trends

We now turn to discuss environmental trends present in the early type population of Cl 0024. For the brighter sample of galaxies with high quality spectra, we can analyze the residuals from the empirical scaling laws presented in § 4, and look for variations with local density, cluster radius, or galaxy luminosity. For the full sample of galaxies to $I = 22.5$ we additionally examine the environmental variations in several key spectral lines.

Paper I in this series found that local density was the primary measure of environment outside of the cluster core, suggesting that infalling groups are the logical unit out of which clusters are built. Looking at the detailed spectral properties of early-types now, it would be useful to determine whether spectral properties depend more closely on local density, as the morphological mix seems to, or on radius. Because we are only tracing a much smaller population of 104 galaxies of a single morphological class, we are unable to make such a distinction reliably. We will, however, present plots of spectral features as a function of both R and Σ_{10} . Because projected radius R is more easily measured than Σ_{10} , we will focus our discussion on radial trends. Anticipating the results, we note that the observed trends with R and Σ_{10} are qualitatively similar.

4.2.1. Fundamental Plane

The high scatter about the FP of Cl 0024, discussed in § 4.1 above, leads us to examine $\Delta \log(M/L_V)$ on a galaxy by galaxy basis. For an individual early type (labeled by subscript i), the evolution in M/L_V with respect to the prediction of the local FP is related to its offset from the local intercept γ according to:

$$\Delta\gamma^i = \log R_e^i - \alpha \log \sigma^i - \beta \mu_V^i - \gamma$$

and

$$\Delta \log \left(\frac{M}{L_V} \right)^i = -\frac{\Delta\gamma^i}{2.5\beta}$$

In Figure 7, we plot $\Delta \log(M/L_V)$ as a function of projected radius and local density. Both plots show a trend toward increased scatter near the cluster core, at small radius and high densities.

In the radial plot, the open triangles overplotted represent the mean $\Delta \log(M/L_V)$ for galaxies within each of the three radial zones delimited by dotted lines: cluster core ($R < 1$ Mpc), transition region ($1 \leq R < 2.4$ Mpc), and periphery ($R \geq 2.4$ Mpc). These three zones were introduced in Paper I, and represent regimes where different physical mechanisms may be effective in transforming galaxies. We see a clear trend of increasingly negative $\Delta \log(M/L_V)$ as we move outward, indicating that galaxies are more luminous for

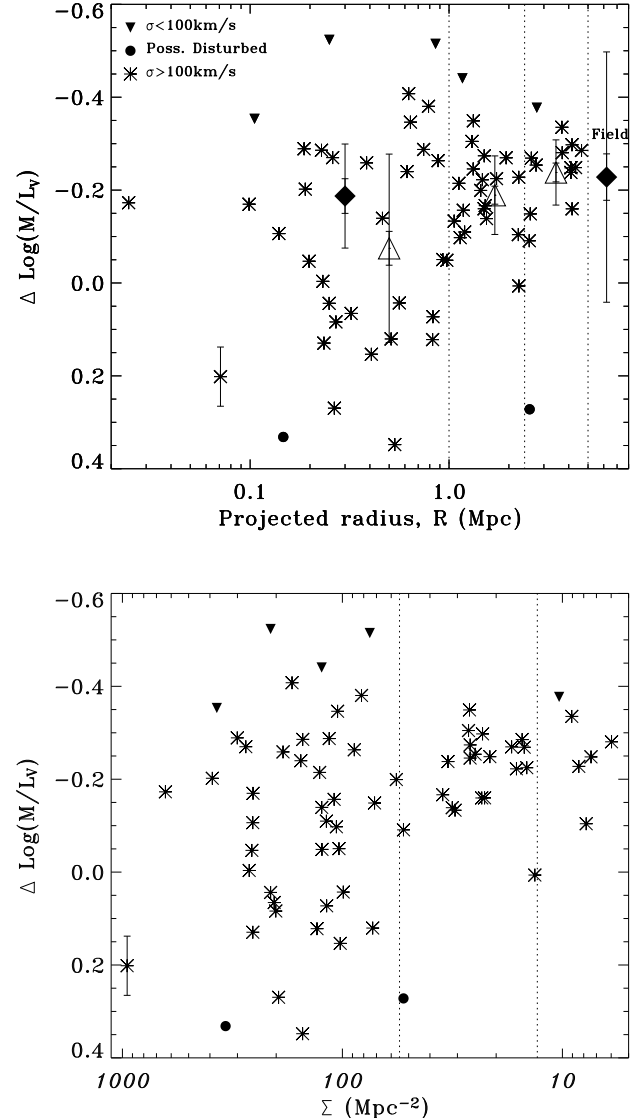


FIG. 7.—Change in M/L_V ratio for galaxies in Cl 0024, with respect to $\langle M/L_V \rangle$ for Coma. Plotted with respect to radius, top, and local density, bottom. Asterisks represent individual galaxies, with a typical error bar shown on a point near the lower left of each plot. For the upper plot, open triangles represent averages for the three radial zones indicated. Large error bars reflect the rms scatter, and small bars are the error on the mean. Filled diamonds are points from van Dokkum & Franx (1996) and Treu et al. (2005b) for cluster core and field, respectively. Dotted lines at 1 Mpc and 2.4 Mpc delimit the three radial zones discussed in the text; corresponding dotted lines in the local density plot represent the mean values of Σ_{10} at 1 Mpc and 2.4 Mpc, respectively.

their mass, and hence appear younger, at larger distances from the cluster center.

Galaxies marked with a filled triangle in Figure 7 have $\sigma < 100 \text{ km s}^{-1}$. These, along with two disturbed-morphology galaxies marked with filled circles, are not included in the calculation of the means for each radial zone. The low- σ galaxies are likely biased toward low M/L_V , due to the selection effect where only the brightest of the small, compact cluster members are within our limiting magnitude.

The solid diamond plotted within 1 Mpc on Figure 7 is the mean $\Delta \log(M/L_V)$ found by van Dokkum & Franx (1996);

it is clear now why our mean value of $\Delta\text{Log}(M/L_V)$ is slightly larger than theirs: the additional contribution from lower M/L_V galaxies in the transition region and periphery boost the mean luminosity evolution we calculate. It is interesting also to note that our new wide-field data bridges the gap between the mass to light ratios typical of cluster cores and those found in the field at this redshift. The other solid diamond plotted in Figure 7, labeled “Field”, is from Treu et al. (2005b), who measured the FP of field galaxies at intermediate redshift. Similar values for the field are reported by Treu et al. (2001a) and van der Wel et al. (2005). While some studies of the field FP at intermediate redshift have reported a slower redshift evolution (e.g. Ziegler et al. 2005; van Dokkum & Franx 2001; Rusin et al. 2003), van der Wel et al. (2005) have shown that most of the discrepancy between studies of field early types can be attributed to differences in analysis methods and selection criteria. Since the reported variations are small on the scale of Figure 7 (less than ± 0.1 in $\text{log}(M/L_V)$), we can be confident that $\langle M/L_V \rangle$ does actually vary with environment at intermediate redshift. This gradient in $\langle M/L_V \rangle$ across the cluster appears to directly reflect the difference in formation history between galaxies in high and low density environments.

Within the cluster core, the scatter in $\Delta\text{Log}(M/L_V)$ is highest, as noted above in § 4. We caution that projection effects could contribute to the apparent scatter near the cluster center, especially if there is a strong gradient in M/L_V with 3D radius, r . However, for any sensible distribution, we would expect that the number of true core members is higher than those at large radii projected upon the core. As we see approximately equal numbers of galaxies both above and below the mean $\Delta\text{Log}(M/L_V)$ in the core, we conclude that projection effects cannot account for the increased scatter. This is confirmed by Kolmogorov–Smirnov tests that compare various simulated distributions of galaxies to our observed distribution.

Similarly, we find no evidence that the high- or low- M/L_V early types in the core are part of an infalling group; $\Delta\text{Log}(M/L_V)$ appears uncorrelated with the velocities or spatial distribution. It has been hypothesized that Cl 0024 is currently undergoing a face-on merger with a large group, as indicated by the double-peaked redshift distribution first reported by Czoske et al. (2002), and replicated in the redshift distribution of Figure 2. However, none of the galaxies on our FP lie in the secondary “Peak B”. While the high scatter may still be related to the subcluster merger, whatever mechanism affects the mass to light ratios of early-types in the cluster core is not apparent in any other measurements.

Although the observed scatter seems at variance with the notion that massive cluster ellipticals are uniformly old and quiescent, if we use the Bruzual & Charlot (2003) SSP models to predict the passive evolution of these galaxies to $z = 0$, the resulting scatter will match that observed locally. Furthermore, the scatter in the field FP reported by Treu et al. (2005b) in this redshift range is larger than in the core of Cl 0024, as expected if the range in ages and star formation histories is greater in the field than in the cluster environment.

There may be two separate populations of E+S0s in the core, then: older galaxies that formed earliest and which have M/L_V already similar to that of local E+S0s, and galaxies with a lower M/L_V which have more recently fallen into the cluster core. While there is no obvious separation between these two groups in Figure 7, we do notice a residual correlation

between $\Delta\text{Log}(M/L_V)$ and σ , in the sense that the most massive, highest- σ cluster galaxies also have the highest mass to light ratios, indicating the oldest stellar populations. This is not a surprising correlation, but it does confirm that the high M/L_V galaxies are typically the oldest and largest found in the cluster. It is also in agreement with a more general trend identified by Treu et al. (2005a), who found that less massive galaxies exhibit a younger luminosity-weighted age than do the most massive ones.

It is important to note, however, that the radial trend observed in $\Delta\text{Log}(M/L_V)$ is not due solely to this “downsizing” relation between galaxy mass and M/L_V . There is still a radial gradient in M/L_V , even when we further restrict our sample to a narrow range of galaxy masses². For example, if we limit our sample to the mass range $10.9 < \text{Log}(M/M_\odot) \leq 11.4$, we observe a significant difference in M/L_V between the cluster periphery and core: $\delta < \text{Log}(M/L_V) > = 0.13 \pm 0.07$. Using field galaxies from the Treu et al. (2005b) sample within this same mass range (and in the redshift range $0.3 < z < 0.5$), we find an offset between the Cl 0024 cluster core and the field equal to $\delta < \text{Log}(M/L_V) > = 0.09 \pm 0.06$. The lower mass limit was chosen because galaxies above $\text{Log}(M/M_\odot) = 10.9$ are negligibly biased due to the luminosity limit of both surveys. The upper mass limit is chosen so that we include only galaxies that are well-represented across the entire cluster, excluding the high-mass galaxies found only in the core.

It makes sense to search for morphological differences between the old and young E+S0s in the cluster core. The existence of the morphology–density relation in Cl 0024 (Paper I) leads us to consider whether the younger, low M/L_V galaxies are preferentially S0s that have recently been created or transformed from spirals. However, when we divide our sample into groups that lie above and below the mean M/L_V in the cluster core, we see no evidence for morphological segregation.

In the second paper in this series on Cl 0024, Kneib et al. (2003, hereafter, Paper II) estimated the global mass to light ratio of the cluster as a function of radius, by combining a mass map based on their gravitational lensing analysis with K_S -band observations which trace the stellar mass. They concluded that the overall M/L of the cluster is remarkably flat, at least within 2 Mpc of the cluster core. (Their result was the same whether they measured total light via K or rest-frame V observations.) At first glance, the radial gradient in M/L_V seen in Figure 7 may appear to contradict the results of Paper II. However, the *cluster M/L* ratio measured in Paper II is much more strongly dominated by dark matter than the *early type galaxy M/L* discussed here, and so variations in mass to light ratios of individual galaxies can be consistent with an overall cluster M/L_V that is constant.

4.2.2. Line Strengths

In the next two sub-sections, we will consider environmental trends in several different indicators of star formation and metallicity, in both our high-quality sample of galaxies and the full sample to $I = 22.5$. It is important to gauge the effect of any recent star formation on the overall M/L_V of these galaxies, to ensure that we can correctly attribute differences in M/L_V to differences in mean galaxy age, rather than the effects of relatively recent and small star forming events. We

² We calculate a galaxy’s dynamical mass, in solar units, according to $M = 5\sigma^2 R_e/G$, which is equal to $M = 1162\sigma_0^2 R_e$, with R_e in pc and σ_0 in km s^{-1} .

also wish to trace the star formation itself, as any significant star formation in early-type galaxies can act as a signpost to the different physical mechanisms that could be at work.

We focus on two key indicators of star formation, the [OII] emission line, and the combination ($H\delta_A + H\gamma_A$), which respectively measure ongoing star formation, and recently completed star formation, as discussed in § 3. Figure 8 plots the equivalent widths of these two diagnostic indices as a function of radius and local density. Solid symbols indicate galaxies with $I \leq 21.1$; we note that some of these brighter galaxies do not have measured velocity dispersions, and so were not included in the high quality sample discussed in previous sections. Open symbols are galaxies in the magnitude range $21.1 < I \leq 22.5$. As we saw with the FP, we note that the strengths of these indices vary in a similar way with both local density and projected radius.

Examining individual measurements of $EW([OII])$, we find a population of galaxies with strong emission, which are concentrated in a narrow range in radius, close to the Virial radius at 1.7 Mpc. The spectra of these galaxies are dominated by emission lines, including [OIII] and several Balmer lines. (See Figure 11). These emission line galaxies are preferentially dim; as denoted by the un-filled pentagons in Figure 8, most are in the magnitude range $21.1 < I \leq 22.5$. Most previous studies have not been sensitive to early-type cluster galaxies at these luminosities and in this radius range, though a recent survey of a cluster at $z = 0.83$ by Homeier et al. (2005) has uncovered a similar population of dim emission-line E+S0s, discussed in more detail in § 5.

What could be the nature of these emission line galaxies clustered in radius? While we leave most of the discussion of this question to § 5, we can quickly address some of the possibilities. Figure 9 shows postage stamp images of each of these active galaxies. The top row contains the three emission line galaxies with $I < 21.1$; one of these may be interacting with a neighbor, though the redshift of the neighboring galaxy is not known. None of the others seem to be undergoing major mergers, so merger-induced star formation is ruled out as a cause of emission. One other bright [OII]-emitter could possibly be a misclassified spiral. We looked at the residuals from surface photometry fits for the rest of these galaxies, but found no other indication of spiral arms. Seven of these ten galaxies are also detected by the $H\alpha$ imaging survey of Kodama et al. (2004), and two of the three non-detections have redshifts that would likely place the $H\alpha$ line outside the bandwidth of the narrow-band filter employed by Kodama et al.

Line ratio tests meant to distinguish between star formation and AGN activity are inconclusive for these galaxies. XMM-Newton observations are available which cover a field including most of these emission line early types: none are associated with an X-ray point source (Zhang et al. 2005), even though the XMM-Newton observations are deep enough to detect any clear-cut AGN with $L_X > 10^{42}$ erg s $^{-1}$. Therefore, while we cannot rule out AGN activity for these galaxies, none are definitively AGN. An interesting hypothesis that we will explore in § 5 is that these galaxies have suffered harassment or disturbances from their interaction with the intra-cluster medium (ICM).

In addition to the emission line galaxies, we see a higher mean $EW([OII])$ at larger radius. Figure 11 shows the coadded normalized spectra of all early-types binned by radial zone; top to bottom, they trace the mean early-type spectrum from the periphery to the core. All galaxies with $EW(OII)$

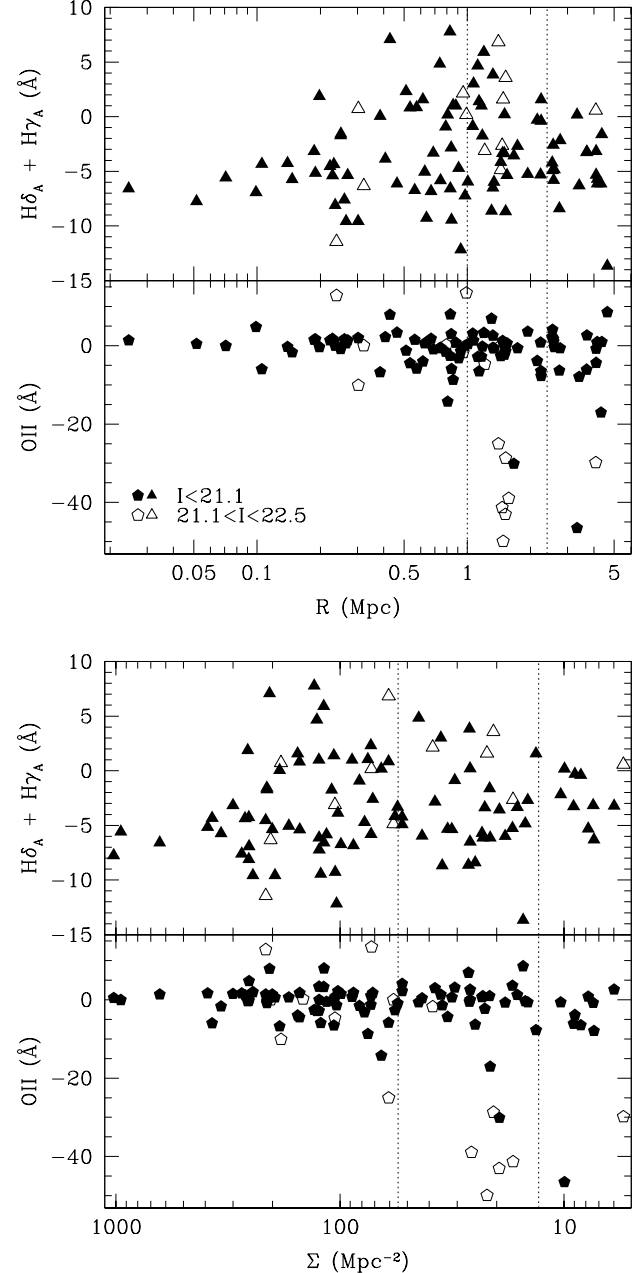


FIG. 8.— $H\delta_A + H\gamma_A$ and [OII] EWs for all E+S0 members as function of radius (top) and local density (bottom). Negative values represent emission in [OII], but can be considered weak absorption for the Balmer lines, due to an effect where the continuum flux in the index sidebands falls completely below the flux in the index bandpass. In the upper plot, dotted lines delineate the core, transition region, and periphery. Dotted lines in the lower plot mark the mean values of the local density at these same radii. Open symbols: $21.1 < I \leq 22.5$. Filled symbols: $I \leq 21.1$.

$< -15\text{\AA}$ were coadded separately; see Figure 11, right. Co-added spectra of ‘normal’ E+S0 members in Figure 11 show an increase in an average galaxy’s OII emission outside of the cluster core. This trend is qualitatively similar to radial gradients in emission line strength seen for samples of cluster galaxies that include all morphologies, both at intermediate (e.g. Gerken et al. 2004) and low redshift (Gómez et al. 2003; Lewis et al. 2002, e.g.).

In Figure 10, we plot the fraction of all E+S0 galaxies with

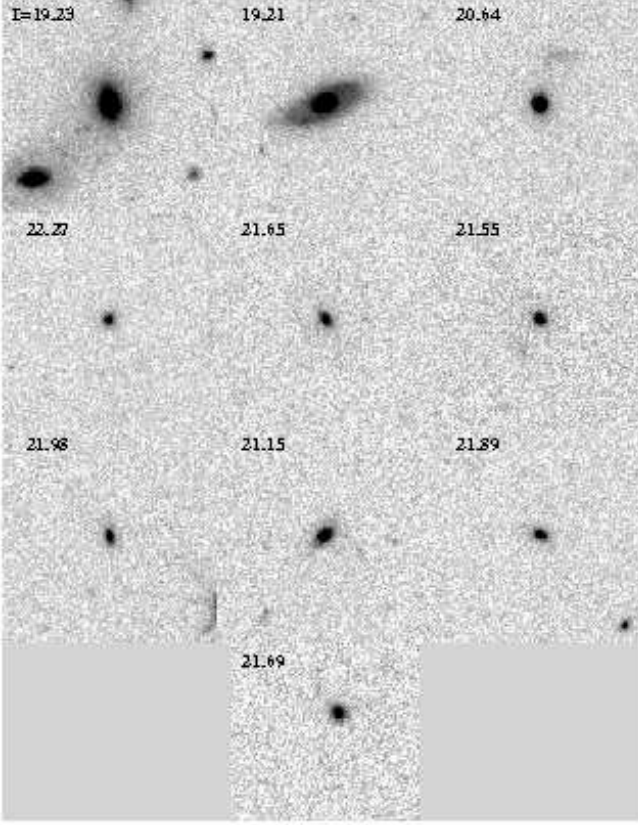


FIG. 9.— Postage stamp images of all galaxies with $\text{EW}(\text{OII}) < -15\text{\AA}$. The top row shows galaxies with $I \leq 21.1$, and the lower rows contain galaxies in the range $21.1 < I \leq 22.5$. Stamps are $10''$ on a side.

$\text{EW}(\text{[OII]}) < -5\text{\AA}$, averaged across each of the radial zones indicated. At all luminosities, it is clear that the fraction of [OII] emitting early types is highest in the cluster periphery and field. Though the fraction of emission line galaxies may be elevated due to selection effects (§ 3), especially at fainter magnitudes, there still exists radial variation within any single magnitude bin. This radial variation holds (in the two brighter magnitude bins) even if we exclude the cluster core, where the fraction of [OII] emitters may be affected by the process causing the strong [OII] emission at the Virial radius.

We see then that both the fraction of galaxies with measurable [OII] emission, and the average strength of that emission rises slightly with radius. This suggests an encounter with the cluster environment which serves to gradually suppress the already low levels of early-type star formation during infall. Another possibility is a simple gradient in galaxy formation age: older early types near the cluster core may simply contain less residual gas available for star formation. However, this scenario is more difficult to reconcile with other studies that have found strong gradients in the overall star formation rates within clusters (e.g. Kodama et al. 2004; Poggianti et al. 1999; Balogh et al. 2000).

Turning now to the Balmer absorption strengths, we see a mix of galaxies in Figure 8 with low to moderate Balmer absorption in the periphery and transition region. These are consistent with the low levels of ongoing star formation indicated by [OII] emission. Almost coincident with the set of strong [OII]-emitters discussed above, we begin to see galaxies with much higher values of $(\text{H}\delta + \text{H}\gamma)$, which appears to decay to-

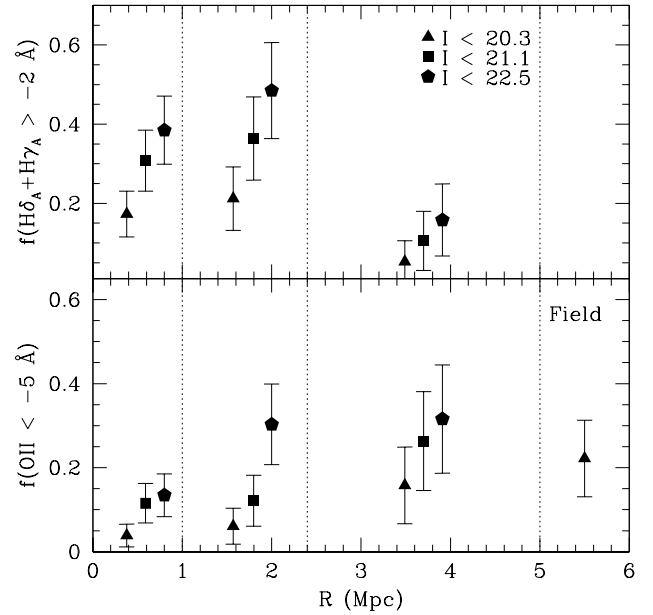


FIG. 10.— Fraction of E+S0 galaxies with $\text{EW}(\text{H}\delta_A + \text{H}\gamma_A) > -2\text{\AA}$, top, and $\text{EW}(\text{[OII]}) < -5\text{\AA}$, bottom, as a function of radial zone. Triangles represent fraction for galaxies with $I < 20.3$. The field value is from Treu et al. (2002). Squares and pentagons are the same measure, but to $I = 21.1$ and $I = 22.5$, respectively.

ward the center of the cluster. If the [OII] emission seen at the Virial radius is, in fact, due to star formation, these galaxies with enhanced Balmer absorption may have undergone a similar burst of star formation in the recent past. The excess absorption then seems to decay away as galaxies migrate further toward the center of the cluster.

Figure 10 confirms that the fraction of early-types with strong Balmer absorption rises dramatically for galaxies in the transition region, and stays high even in the cluster core. Since so few early types in the periphery show similarly high Balmer absorption, there is likely an interaction with the cluster environment that triggers both the enhanced OII emission and the longer-lived Balmer absorption that we observe. We will discuss the the possible link between these two populations of E+S0s in more detail in § 5.

We additionally searched for environmental trends in the metal line indices Mg_2 , Mg^b , and $[\text{MgFe}]'$, but detect no significant trends. In contrast with the correlation between, e.g., $[\text{MgFe}]'$ and σ , it seems that the overall metallicity of early-type galaxies is not dependent on environment, but mainly on the galaxy's formation history, as traced by σ . While the highest values of $[\text{MgFe}]'$ that we measure tend to be seen in galaxies within the Virial radius, this is simply a reflection of the fact that most of the massive cluster galaxies with highest velocity dispersion are also located in the cluster core.

4.2.3. Residual Correlations

In addition to the environmental trends in spectral line strengths discussed above, we can probe environmental effects on the early type population even more sensitively by examining the residuals from the $[\text{MgFe}]' - \sigma$ and Balmer- σ relations presented in § 4.1. In Figure 12, we plot $\Delta[\text{MgFe}]'$ and $\Delta(\text{H}\delta + \text{H}\gamma)$ versus projected radius. Similar to what we saw in Figure 8, we see a population of galaxies with enhanced

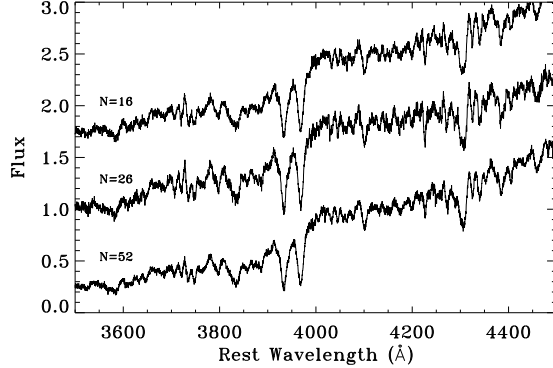


FIG. 11.— Coadded spectra. The right panel shows coadded spectrum of E+S0 members with $\text{EW}(\text{OII}) < -15\text{\AA}$. The full spectrum is on top, with an excerpt below it which shows OII emission, Ca H & K, and Balmer absorption lines in more detail. The left panel shows coadded spectra for all other E+S0 members, divided by distance from cluster core. From top to bottom: periphery, transition region, and cluster core. Wavelengths in rest frame.

Balmer absorption within the Virial radius at 1.7 Mpc. In this plot, though, we are able to remove the effects of galaxy mass by looking, in effect, at galaxies that have excess Balmer absorption *compared to other galaxies at the same velocity dispersion*. This is clear evidence, then, that the observed Balmer excess is an environmental effect, and not simply due to a dual correlation between line strength–mass and mass–cluster radius.

In the top panel of Figure 12, where we plot $\Delta[\text{MgFe}]'$, galaxies that also exhibit $\Delta(\text{H}\delta+\text{H}\gamma) > 2\text{\AA}$ are marked with red squares. Virtually all of the galaxies with anomalously low $[\text{MgFe}]'$, which we made note of in Figure 6, belong to this population of Balmer-strong galaxies. For the first 1 Gyr after a burst of star formation, we would in fact expect that the A-stars causing the enhanced Balmer absorption would also tend to fill the metal absorption lines with emission, as these lines are much weaker in A-stars than they are in the older stars making up the bulk of the stellar population. In fact, Tantalo & Chiosi (2004) suggests that a young stellar population has just this effect: $[\text{MgFe}]'$ is very low for mean ages less than 2 Gyrs, while $H\beta$, and presumably the other Balmer indices are enhanced.

We find no evidence that any of Mg_2 , Mg^b , $[\text{OII}]$, or any Balmer lines are correlated with the residuals from the FP, $\Delta\text{Log}(M/L_V)$. Nor is there evidence that the residuals from any of the Mg– σ , or Balmer– σ relations are correlated with $\Delta\text{Log}(M/L_V)$. This indicates that recent perturbations to the stellar population of an early-type are somewhat decoupled from its overall mass to light ratio. While the FP, $[\text{MgFe}]'-\sigma$, and Balmer– σ relations establish a clear link between the formation histories of E+S0s and their current appearance, the lack of correlation between residuals indicates that environmental effects play a relatively minor role in determining M/L_V . The initial time of formation and mass-assembly history seem to be the dominant factors.

4.3. Luminosity Trends

Figure 10 reveals that there is a luminosity trend in the fraction of E+S0 galaxies with $\text{EW}([\text{OII}]) < -5$, as well as the fraction with enhanced Balmer absorption. For the brightest galaxies, $I < 20.3$, the fraction of $[\text{OII}]$ -emitters decreases monotonically, from the field measurement of Treu et al. (2002) to the cluster core. However, when we include slightly dimmer galaxies, to $I = 21.1$, we see an enhanced fraction

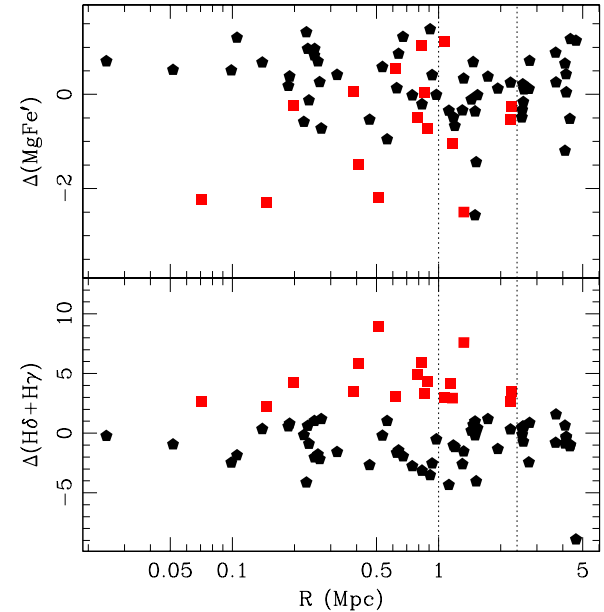
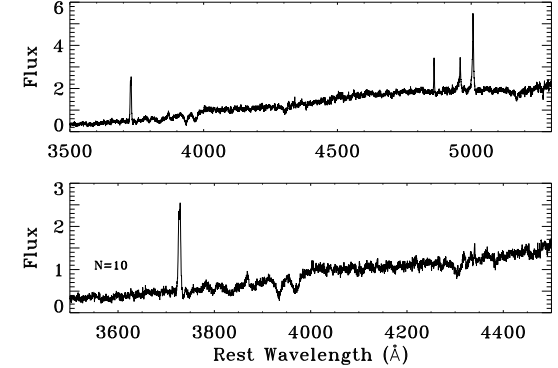


FIG. 12.— Residuals from the $[\text{MgFe}]'-\sigma$ and $(\text{H}\delta+\text{H}\gamma)-\sigma$ relations. The interaction with the environment has spurred increased star formation within the Virial radius. Galaxies that lie above ~ 2 in the bottom panel have Balmer absorption that is unexpectedly strong for their velocity dispersion. Similarly, galaxies with $\Delta[\text{MgFe}]' < -1$ are showing unexpectedly weak metal lines. In both panels, galaxies with $\Delta(\text{H}\delta+\text{H}\gamma) > 2.0$ are marked with red squares.

of emitters in the cluster periphery, though $[\text{OII}]$ emission is still rare within 2.4 Mpc. Now including our full sample to $I = 22.5$, the fraction of star-forming galaxies in both the transition region and periphery are higher than expected. In the transition region, the jump represents the addition of the dim but strongly emitting galaxies discussed above (which have a mean magnitude of $I = 21.1$). The overall trend suggests that the star formation observed in the outskirts of this cluster is suppressed earliest in the largest and brightest E+S0s.

A similar trend is seen in the fraction of early types with $(\text{H}\delta+\text{H}\gamma) > -2\text{\AA}$. As discussed above, we see a jump at all luminosities in the fraction of Balmer-strong galaxies within the Virial radius, possibly due to the same mechanism that causes

the enhanced [OII] emission. But within each radial zone, the fraction of galaxies with prominent Balmer absorption increases with increasing magnitude; the mean magnitude of all such Balmer-strong early types is $I = 20.3$. However, unlike [OII], which probes current star formation only, the Balmer lines are also sensitive to the stellar population age. This gradient in Balmer strength with luminosity could simply reflect an earlier formation time for the brightest galaxies, regardless of local environment.

The brightest galaxies in our sample ($I < 20.3$) follow the FP and show few signs of star formation. Similarly, galaxies to $I = 21.1$ lie on the FP (albeit with a high scatter) and exhibit star formation mainly in the periphery. Perhaps star formation is quenched early during infall of these galaxies, with mostly passive luminosity evolution from that point. Because the dimmest galaxies seem to undergo the most prominent bursts of star formation (though AGN activity has yet to be ruled out), it seems that the physical mechanism responsible affects smaller galaxies more dramatically than larger galaxies. Of course, the elevated fraction of galaxies with strong Balmer absorption demonstrates that all early types, bright or dim, are affected to some degree. When evaluating the physical mechanisms that lead to the observed environmental evolution, we must also consider this dependence on luminosity.

5. DISCUSSION

Having presented our results in the previous section, we now proceed to a more comprehensive discussion of our findings trying to put together the various pieces of information and reconstruct the evolutionary process, its timescales and the physical mechanisms driving it. First, in Section 5.1, we will combine the radial trends obtained so far and discuss them jointly. Then, in Section 5.2 we will present a simple infall model which indicates that a common physical mechanism may cause several of the radial trends seen in various subpopulations of E+S0s. In Section 5.3 we discuss the physical mechanisms at work and conclude that our study of early-type galaxies has revealed the action of at least two different environmental processes: starvation and/or galaxy harassment is quenching low-level star formation over a long timescale in early-types beyond the cluster core, while harassment and/or interactions with shocks in the outer parts of the ICM are producing the sudden bursts of star formation observed in small E+S0s around the Virial radius.

5.1. Radial trends and star formation timescales

In the residuals from the Fundamental Plane, we have observed a gradient in the mean mass to light ratios of E+S0s, allowing us to observe the transition from the oldest, highest M/L_V galaxies in the cluster core, to the galaxies in the cluster periphery with younger luminosity-weighted ages, nearly matching the values of M/L_B seen in field E+S0s (Treu et al. 2001a, 2005b; van der Wel et al. 2005). The scatter in the FP residuals is unexpectedly high within the inner 1 Mpc of the cluster, but the FP appears tighter outside of this radius. Direct measurements of spectral line strengths (Figure 8) and the fraction of [OII]-emitting early-types (Figure 10) both reveal a mildly declining star formation rate within early-types, from the field toward the cluster core. This is interrupted by an interaction at the Virial radius that causes enhanced [OII] emission in a population of small, dim early types, along with enhanced Balmer absorption and depressed [MgFe]' absorption strength for a population of larger, typical cluster E+S0s.

In Figure 13, we combine the previously shown radial trends in $\Delta \log(M/L_V)$, $\Delta(MgFe')$, $\Delta(H\gamma+H\delta)$, and $\text{EW}(\text{[OII]})$ into a single plot. As in Figure 12, in the top three panels we indicate every galaxy exhibiting high Balmer absorption with a red mark. Likewise, all galaxies with significant [OII] emission in the bottom panel are plotted with open symbols in each panel. While the galaxies with unexpectedly low [MgFe]' correlate with the Balmer-strong galaxies, as mentioned in § 4 above, there is no similar correlation with $\Delta \log(M/L_V)$. We see some Balmer-strong galaxies at both low and high M/L_V , which indicates that the star formation causing the enhanced Balmer line strengths does not drive the variations in M/L_V that we observe; the bursts of star formation are perhaps too minor to affect the overall M/L_V of the galaxy, at least to levels detectable in our data.

Briefly, we recap the characteristic timescales for changes in each of the quantities plotted. [OII] emission traces the instantaneous rate of star formation, so that the observed strong [OII] emitters mark the location of a “hot spot” of current star formation at 1.7 Mpc radius (though we emphasize that these objects are not spatially clustered). Enhanced Balmer absorption will persist for about 1 Gyr after a burst of star formation, and so there is a time lag of < 1 Gyr between the termination of star formation in these galaxies and the time when we observe them. Changes in M/L_V should persist for a similar amount of time after a recent burst of star formation (until the luminous A stars begin to disappear), though we expect that M/L_V is less sensitive to low-level star formation because it depends more closely on the integrated stellar light of the galaxy, which changes by a smaller amount than the strong spectral lines.

5.2. A simple infall model

We have so far presented evidence for a seemingly abrupt encounter with the environment that triggers star formation in early-types at or near the Virial radius, along with a moderate decline in star formation from the periphery to the core, and a trend in M/L_V that suggests that the stellar populations of early types at larger radius are younger. In this section we present a simple infall model as a tool to compare the timescales and strengths of several of the observed features in the early-type population. Specifically, we wish to examine the possibility that both the galaxies with strong [OII] emission and those with excess Balmer absorption could be caused by a common physical process. And while we have shown in § 5.1 that the FP residuals, $\Delta \log(M/L_V)$, do not correlate with the Balmer-strong galaxies, we will also use this simple infall model to constrain the level of variation in M/L_V that could be induced by the environment.

In this idealized model, we follow an early-type galaxy as it proceeds toward the cluster center evolving passively, until it reaches the Virial radius where it undergoes a short burst of star formation (adding 1% to the total stellar mass, 200 Myrs of duration). After the burst, the galaxy continues its infall evolving passively. For this model we use the prescription of Paper I to convert from infall time to cluster projected radius: assuming that the galaxy is on its first infall toward the cluster, it begins with a small velocity at $R = 5$ Mpc and accelerates freely toward the cluster potential.

The observable properties of this model are then computed using stellar population synthesis models by Bruzual & Charlot (2003) to compare with observations. Although this is clearly a simplified model – for example it neglects “backsplash” (Gill et al. 2005; Ellingson 2004), i.e. the

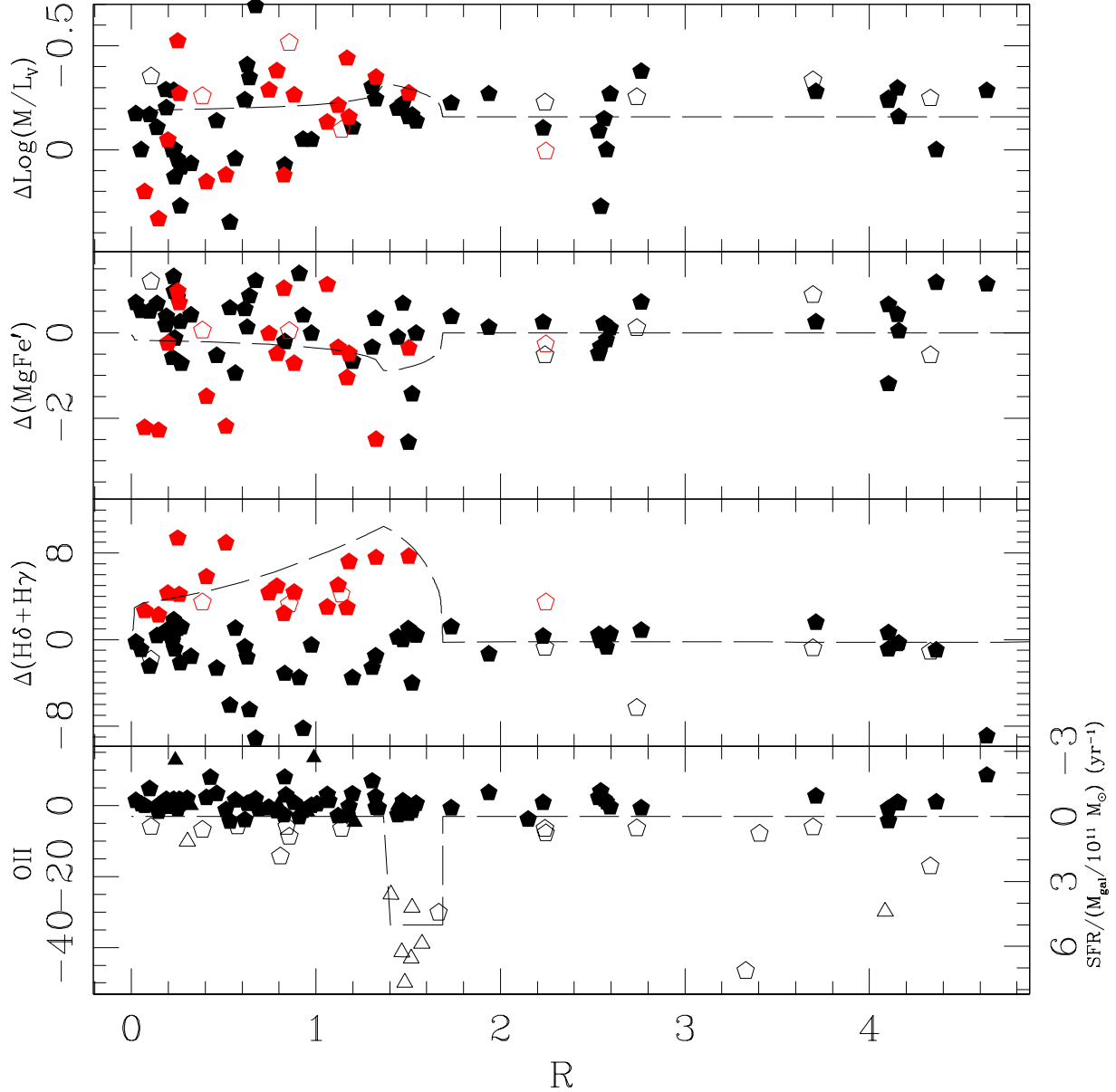


FIG. 13.— Radial trends in the residuals of dynamical relations. From top to bottom, $\Delta \text{Log}(M/L_V)$, $\Delta(\text{MgFe}')$, $\Delta(\text{H}\delta + \text{H}\gamma)$, and $[\text{OII}]$ vs. R for reference. Galaxies brighter than $I = 21.1$ are marked with pentagons, and triangles represent galaxies in the range $21.1 < I \leq 22.5$. In the top three panels, we indicate every galaxy exhibiting high Balmer absorption ($\Delta(\text{H}\delta + \text{H}\gamma) > 2 \text{\AA}$) with a red mark. Likewise, all galaxies with $[\text{OII}] < -5 \text{\AA}$ in the bottom panel are plotted with open symbols in each panel. Overplotted on each plot is the track of a simple early-type galaxy model, as the galaxy falls freely from the outskirts of the cluster, and has an encounter at the Virial radius which triggers a starburst of duration 200 Myrs, totaling 1% of the galaxy's mass.

fact that especially in the cluster center, and even out to two virial radii, some galaxies might not be on their first approach toward the cluster (see discussion in Paper I), and it is a closed boxed model, i.e. there is no provision for galaxies being transformed into E+S0s during the infall – we will show that this model reproduces the strengths and timescales of many of the observed features and provides useful guidance to interpret the observations.

The predictions of the model are shown as a dashed line in Figure 13. Specifically, we plot the difference in $\Delta \text{Log}(M/L_V)$, $\Delta(\text{MgFe}')$, $\Delta(\text{H}\gamma + \text{H}\delta)$, and star formation

rate (SFR) between the infalling model galaxy and an identical model without the starburst. Since we are interested only in the predicted change in line strengths due to a recent star formation event, the proper quantity to plot is this difference between the index strengths predicted by the passive model and the one with a small starburst overlayed. We emphasize that the model track for $\Delta \text{Log}(M/L_V)$ is meant to replicate only the change in M/L_V caused by a small starburst, and does not account for the radial gradient in $\Delta \text{Log}(M/L_V) >$ seen in the data.

To calibrate the star formation rates predicted by the mod-

els to the [OII] equivalent widths observed, we used SFRs derived by Kodama et al. (2004, and private communication) from their deep $H\alpha$ images, according to the procedure outlined in § 3.4.

The choice of a 1% starburst produces a SFR and [OII] equivalent width equal to that observed in the largest/brightest of our low-luminosity [OII] emitting galaxies, which we estimate to have a stellar mass up to around $5 \times 10^{10} M_\odot$ (See § 3.4). The 200 Myr timescale approximately matches the spread in cluster radius over which we see these [OII] emitters. The stellar mass associated with the starburst could vary with galaxy size and need not add up to 1% of the galaxy mass. For our [OII] emitters, the luminosities and equivalent widths imply that up to a 5% burst could be involved, depending on its duration. However, 1% represents a good upper limit for the larger galaxies with enhanced Balmer absorption, as we would otherwise expect to observe “post-starburst” k+a spectra; the excess Balmer absorption is not strong enough to place any in this category.

Examining the track of the model in Figure 13, it is remarkable how well the expected change in Balmer line strength matches the observations in both maximum strength and in the time it takes this enhanced absorption to decay away. This lends strength to our contention that the enhanced Balmer absorption and the high [OII] emission are reflections of the same physical process.

We also observe a dip in the strength of $[\text{MgFe}]'$ just where we would expect it, though the magnitude of this dip does not seem great enough to account for the observed $[\text{MgFe}]'$ decrement. This may simply be a deficiency in the Bruzual & Charlot (2003) models, as the observed values of $[\text{MgFe}]'$ span a larger range than could be predicted by the models at any SSP age or metallicity. In contrast, the models easily account for the full range of observed Balmer line strengths. Therefore, changes in $[\text{MgFe}]'$ due to a small starburst could be under predicted by the Bruzual & Charlot (2003) models.

We note that the population of [OII] emitters observed cannot evolve directly into the population of galaxies with strong Balmer lines, though they could still be indicators of the same physical mechanism. The Balmer-strong E+S0s are brighter and larger in effective radius, and any fading of the [OII] emitters would only increase the difference between these populations. Since they are near our spectroscopic magnitude limit, we would not expect to observe faded remnants of the [OII] emitting galaxies. On the other hand, the lack of bright early types with strong [OII] emission might arise because the timescale for the Balmer lines to decay (1 Gyr) exceeds the starburst timescale (200 Myrs), so that we would not expect to observe more than one of the emission line progenitors of these Balmer-strong galaxies. This is partly due to the overall smaller number of bright E+S0s observed within the transition region (1–2.4 Mpc), in comparison to the ~ 50 observed in the cluster core.

To further examine our hypothesis that the [OII]-emitting and Balmer-strong galaxies are caused by the same environmental interaction during infall, we can examine the 2D spatial distribution of these galaxies. In Figure 14, we plot [OII] emitters in blue and early-types with strong Balmer absorption in red, on top of the overall distribution of cluster members from the combined spectroscopic and photometric redshift catalogs. The [OII] emitters and Balmer absorbers follow the overall distribution of cluster members closely, lying mostly along the major axis of the cluster (stretching from the

overdensity NW of the cluster core through to the SE side of the core). Though the [OII] galaxies perhaps extend in a larger arc at ~ 1.7 Mpc, their small number makes it difficult to determine their azimuthal distribution. The distribution supports the idea that they have been perturbed during infall, as this is most likely occurring predominantly along the NW to SE path.

Turning to the top panel in Figure 13, it seems that the small starbursts at the Virial radius cannot alter the overall M/L_V of early types by a large enough amount to account for the large scatter that we see in the cluster core. It seems that there must simply exist a mix of older, high M/L_V galaxies and more recently arrived low M/L_V galaxies in this region. On the other hand, the triggered star formation may help prolong the length of time that an infalling E+S0 remains at low M/L_V after reaching the cluster core. This could possibly explain why the scatter in M/L_V seen in this cluster is so much higher than that observed in Cl 1358+62 at $z = 0.33$ (Kelson et al. 2000b); the mechanism causing this star formation in Cl 0024 might not be active or significant in all clusters at this redshift.

While the simple model presented here does not attempt to account for the observed radial gradient in M/L_V , we note that the difference in $\text{Log}(M/L_V)$ between a galaxy at 5 Mpc radius, of age 2.7 Gyr, and that same galaxy 5 Gyr later (corresponding to the total free-fall time to the cluster center), is equal to -0.35. This is nearly identical to the observed difference in $\text{Log}(M/L_V)$ between the mean value in the periphery, and the M/L_V of the oldest galaxies in the core. While the galaxies in the periphery are almost certainly not this young, the observed gradient in M/L_V seems consistent with a difference in formation age (or in time since the last major burst, c.f. Bower et al. 1998 and Treu et al. 2005b) of a few Gyrs between cluster periphery and core. A gradient in formation age, then, is a viable explanation for the M/L_V gradient we observe, though the gradual decline in star formation that we observe could also be important in generating the M/L_V gradient.

Having suggested that the observed spectral features of our early-type sample are due to a small starburst, it is natural to ask if such a burst is realistic; in other words, do E+S0s at redshift ~ 0.4 contain enough residual gas to undergo such episodes of star formation? According to Bettoni et al. (2003), the fraction of molecular gas detected in local “normal” early type galaxies (i.e. showing no signs of current or recent interaction or dwarf cannibalism, but otherwise selected across all local environments), can approach 1% of the total stellar mass (with typical values ranging from 0.05–0.5%). At intermediate redshifts, some field E+S0s have peculiar color gradients that may indicate recent star formation (e.g. Menanteau et al. 2004). Allowing for the possibility of faint, undetected interaction features in our much more distant sample, as well as the expected decrease in the remnant molecular gas in ellipticals since $z = 0.4$, we expect that a small burst of star formation of up to 1% is entirely plausible for early-type galaxies in Cl 0024. Additional evidence comes from the observation (e.g. Treu et al. 2005b; Bressan et al. 1996) that the combinations of spectral line strengths observed in early-type galaxies are best explained if most early-types have undergone secondary episodes of star formation at some point in their past; the Balmer-strong galaxies observed here could possibly have undergone such secondary bursts in the last 1 Gyr.

5.3. Physical Mechanisms

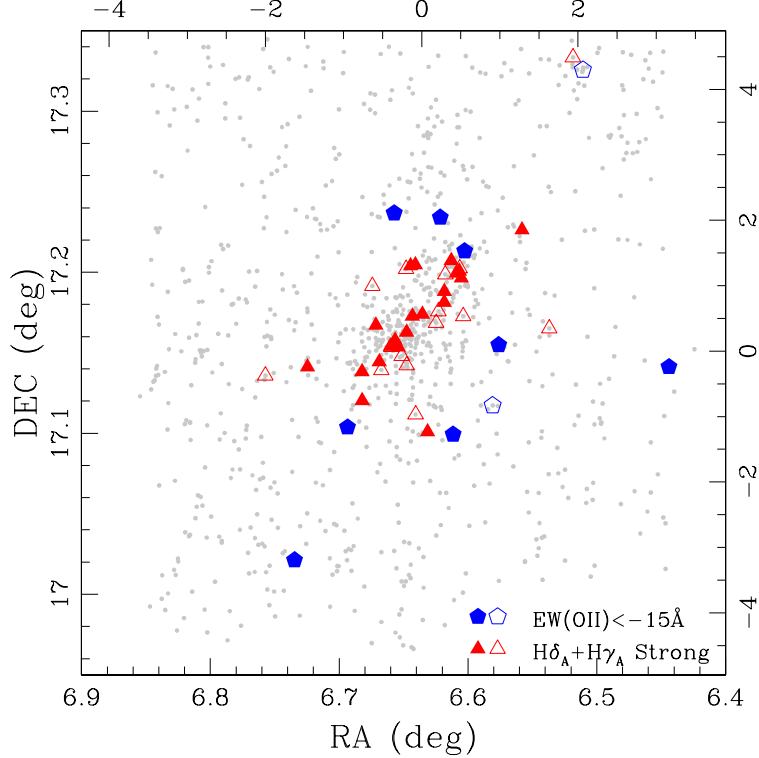


FIG. 14.— Spatial distribution of [OII] emitters and galaxies with excess Balmer absorption, in comparison to the overall distribution of cluster members in the combined spectroscopic and photometric (Smith et al. 2005) redshift catalog (gray dots). Blue pentagons are strong [OII] emitters, with two open symbols marking the merger system and possible spiral interloper seen in Figure 9. Filled red triangles mark galaxies where the Balmer- σ residuals are $\Delta(H\delta + H\gamma) > 2\text{\AA}$, and unfilled triangles represent galaxies without measured velocity dispersions, with $\text{EW}(H\delta_A + H\gamma_A) > -2\text{\AA}$. Top and right axes show projected radius from the cluster center, in Mpc.

The early-type galaxies in Cl 0024 have proven to be effective signposts for identifying two possible forms of environmental evolution in this cluster, but can we identify the physical processes responsible? We observe a slow decline in remnant star formation from the field/periphery to the core which may indicate a physical mechanism at work which slowly quenches star formation. Seemingly overlaid on top of this mild trend is a nearly-instantaneous interaction that triggers a small burst of star formation in many of these early-type galaxies at the virial radius.

First, we address physical mechanisms that could be responsible for the gradual decline in star formation rate toward the cluster core, best illustrated in Figure 10. In analyzing the cause of the observed decline, we must also consider the morphology-density (T- Σ) relation observed in Cl 0024. In Paper I, it was argued that the existence of the T- Σ relation across several orders of magnitude in projected local density indicates that whatever process causes the morphological segregation of galaxies by environment, it acts slowly. The slow “starvation” (See Paper I) of galaxies during infall is consistent with the existence of the T- Σ relation, as is the action of galaxy harassment (Moore et al. 1996, 1999; Moore, Lake & Katz 1998).

Starvation encompasses several physical mechanisms that all serve to slowly deprive a galaxy of cold gas available for star formation. For example, thermal evaporation of the galaxy interstellar medium (ISM) by interaction with the hot cluster ICM (Cowie et al. 1977), or turbulent and viscous stripping of the ISM (Nulsen 1982; Tonizazzo & Schindler 2001) are two possible causes of starvation. Either of these

processes could be acting in Cl 0024, and are consistent with both the observed gradient in star formation rate and the existence of the T- Σ relation.

Kodama et al. (2004), however, argue that the truncation of star formation in cluster galaxies must be rapid, based on their observation that the $H\alpha$ luminosity function does not vary with environment. Both our paper and theirs find a similar decline in the *fraction* of star forming galaxies, but they do not observe a decline in the mean strength of emission. The discrepancy may be due to the different levels of star formation probed: the low levels of remnant star formation in the early-type population discussed here may be quenched slowly, while a separate physical process (such as harassment) could rapidly decrease the moderate star formation observed by Kodama et al. (2004), which occurs mostly in the spiral population. Combined with a longer timescale for morphological transformation, this could lead to the “passive spirals” they discuss.

Paper I also argued that the existence of the T- Σ relation means that the morphological mix is set by the pre-cluster environment: the overall formation history within assembling groups is the dominant factor in determining the morphological mix seen in the cluster. This view is consistent with the trend we observe in the M/L_V ratios of cluster early-types. We find that the differences in M/L_V must arise partially out of variations in the mass-assembly history of early-type galaxies, though the radial trend in $\langle \log(M/L_V) \rangle$ may also reflect the quenching of remnant star formation during infall.

Interrupting the slow decline in star formation are the small bursts of star formation we observe. Rapidly acting mecha-

nisms that could trigger such a burst include galaxy harassment or some encounter with the ICM. As noted in § 4, major mergers are ruled out because the galaxies seem to be in low density regions, and all but one of the galaxies involved show no visual evidence for such a disturbance.

Galaxy harassment becomes important near the Virial radius as both galaxy crowding and the typical velocity of an interaction become high enough. (See Paper I.) Further, it is a rapid interaction, and the galaxy that triggers one of our observed starbursts can quickly move away from the vicinity of the starburst galaxy. Moore et al. (1999) present simulations of the harassment of small Sc/Sd spiral galaxies as they fall into the cluster. Such galaxies can be quickly transformed into objects that appear to have an early-type morphology. These harassment remnants are small objects ($R_e = 1 - 3$ kpc), similar to our observed [OII] emitters, and could represent the origin of the large population of dwarf spheroidals observed in clusters today. In addition, Moore et al. (1999) predict that harassment would drive the gas within a spiral toward the galaxy's center, thus providing a natural mechanism for fueling the starbursts (or AGN) we observe.

If these are the remnants of harassed spirals, they may not be on their first infall into the cluster; the timescale for passage from the cluster core back out to the virial radius may be short enough (< 1 Gyr) that star formation induced by interactions with large ellipticals in the cluster center could still be visible. A possible explanation, then, for finding them preferentially at the virial radius could be that this is near the apse of their orbit within the cluster.

Under the harassment scenario, we speculate that the population of Balmer-strong galaxies could represent the large cluster ellipticals which cause the harassment, perhaps cannibalizing young stars from smaller harassed galaxies. Alternatively, they could be undergoing harassment themselves, albeit with a much smaller gas reservoir and a correspondingly smaller episode of star formation.

Ram-pressure stripping or triggering of star formation has been thought to be effective only much closer to the cluster core, and should not be significant near the Virial radius where the environmental interaction is taking place. However, recent work on large-scale shocks and particularly the Virial shock—the shock boundary between the hot, dense ICM and the colder, diffuse infalling gas from outside the cluster—suggests that a galaxy passing through this shock boundary could be given enough of an impulse to trigger stripping of HI gas and the collapse of any molecular clouds (Evrard 1991; Quilis et al. 2000; Ryu et al. 2003; Furlanetto & Loeb 2004). Particularly relevant to Cl 0024 is the work by Roettiger et al. (1996). They showed that a merger between two clusters or sub-cluster clumps can cause powerful shocks to propagate through the ICM. As the redshift distribution of galaxies in Cl 0024 is double-peaked (Czoske et al. 2002), indicating a large infalling group or sub-cluster, such strong shocks could be responsible for the triggered starbursts we observe. If this is the case, we would not expect to see such bursts in other clusters with more regular structure.

Our sample of 104 E+S0s contains only four galaxies from the smaller Peak B of the redshift distribution in Cl 0024 (Figure 2), so we are unable to more carefully explore possible differences between early type galaxies in these two peaks. But in the local universe, Poggianti et al. (2004) finds a population of star forming dwarf galaxies that lie along contours in the X-ray substructure of the Coma cluster. It is possible that the [OII] emitters in Cl 0024 lie along similar boundaries

in the cluster substructure, but the nearly face-on orientation of the merger between Peak A and Peak B makes testing this hypothesis difficult. In this scenario, the existence of Balmer-strong galaxies interior to the Virial radius would imply that some sort of boundary shock between Peak A and Peak B has persisted for at least ~ 1 Gyr, the timescale for the excess Balmer absorption to decay away.

Our small population of strong [OII] emitters is a signpost to an important physical interaction, and is not a peculiarity unique to this cluster. A similar population of dim, compact, E+S0s with [OII] emission has also been reported by Homeier et al. (2005), for a galaxy cluster at $z = 0.84$. While the cluster they study is not virialized, the [OII] emitters they observe seem to reside in a region outside of the contours of the cluster X-ray emission. And work by Ruderman & Ebeling (2005) examining the radial distribution of X-ray point sources in the MACS sample of clusters has uncovered a prominent spike in the number of cluster AGN detected in the area around the Virial radius (~ 2.5 Mpc in the clusters studied). These AGN may be stimulated by the cluster environment via the same physical mechanism causing the [OII]-strong early-types. Therefore, even though they only represent a small fraction of the total mass and star-formation in clusters, these galaxies warrant further study of their role as indicators of environmental interaction.

While the exact physical mechanisms responsible for the environmental evolution are still not known, further work on this cluster, and a similar planned study of the X-ray bright cluster MS 0451-03 at $z = 0.54$ may allow us to determine which processes are dominant. Analyzing the star formation rates and rotation curves of spirals in Cl 0024 may help us trace the gradual decline in star formation rate hinted at here, as star formation in spirals is in general much more vigorous than in the early types studied so far. Other authors have found similar declines in the star formation rate in spiral populations of clusters at intermediate redshift (Abraham et al. 1996b; Balogh et al. 1999; Balogh et al. 2000). Rotation curves have also been used to study variations in the kinematics and mass to light ratios of spirals, in distant clusters by, e.g., Bamford et al. (2005); Ziegler et al. (2003); Milvang-Jensen et al. (2003), and in Cl 0024 by Metevier & Koo (2004).

Likewise, the X-ray luminosity of MS 0451 is much higher than that of Cl 0024. If shocks in the ICM really do cause the bursts of star formation observed in early types near the Virial radius, then we should see a similar or even stronger effect in MS 0451, but at a higher radius. If the strength of the ICM shocks in Cl 0024 is enhanced by the sub-cluster merger, however, we might expect to see no starbursting early types at all in MS 0451. The importance of galaxy harassment should be nearly the same between the two clusters, so we would expect to see similarly strong starbursts in MS 0451 if the Cl 0024 bursts are due to harassment.

6. SUMMARY

In this paper we have presented the results of an extensive spectroscopic survey of the cluster Cl 0024+1654, undertaken with DEIMOS on *Keck II* and LRIS on *Keck I*. We examine the detailed spectral and photometric properties of cluster early types across an area 10 Mpc in diameter. The principal goal of this wide area survey is to examine variations in galaxy properties with local environment, in order to identify the physical processes that may affect the star formation properties or morphological characteristics of

infalling galaxies. In this paper, we have used the early-type galaxy population as sensitive indicators of interaction with the cluster environment. Our main observational results are:

1) Combining our new redshift survey of nearly 1000 galaxies with previous work on this cluster, we present a comprehensive redshift catalog for Cl 0024, consisting of 1394 unique objects with redshifts, of which 486 are cluster members. From our survey, we select a sample of 104 E+S0 cluster members brighter than $I = 22.5$, for which we can measure spectral line indices. For a subsample of 71 of these galaxies, with high quality spectra available and $I \leq 21.1$, we also measure reliable velocity dispersions and analyze surface photometry from their *HST* images.

2) By constructing the Fundamental Plane of Cl 0024, we observe that E+S0s at $z \sim 0.4$ still have old stellar populations; from a comparison with the FP of the Coma cluster ($z \sim 0.02$), we infer an evolution in mass to light ratio of $\Delta(\log(M/L_V)) = -0.14 \pm 0.02$. While the mean change in M/L_V is in line with that expected by passive evolution of an old stellar population, the high scatter of 40% in M/L_V suggests a more complex assembly history for this cluster. The high scatter may be an effect of the cluster merger currently underway (Czoske et al. 2002), though at least one other intermediate redshift cluster (Wuyts et al. 2004) exhibits a similarly high scatter.

3) We observe radial trends in the mass to light ratios of individual early types, with the oldest galaxies located in the cluster core ($\langle \Delta \log(M/L_V) \rangle_{R < 1 Mpc} = -0.13 \pm 0.04$). Galaxies seem to be younger at higher radius, with E+S0s in the cluster periphery ($\langle \Delta \log(M/L_V) \rangle_{R > 2.4 Mpc} = -0.24 \pm 0.02$) nearly matching the values of M/L_V seen in the field at this redshift (Treu et al. 2005b). We therefore have bridged the gap between the observed properties of cluster and field early types at intermediate redshift. Similar trends are seen as a function of local density. Some fraction of this radial gradient could be caused by the “downsizing” effect described by, e.g., Treu et al. (2005b); Holden et al. (2005); van der Wel et al. (2005). But even when we select a subsample of galaxies within a narrow range of galaxy mass ($10.9 < \log(M/M_\odot) \leq 11.4$), we observe a significant difference in age (or time since the latest burst) between galaxies in the cluster periphery and core, equivalent to $\delta \langle \log(M/L_V) \rangle = 0.13 \pm 0.07$. Physically, this trend could be explained by some combination of a gradient in formation age and variations in recent star formation, perhaps modulated by “starvation”.

4) Around the virial radius, we observe a number of small galaxies undergoing a burst of star formation, indicated by strong [OIII] emission. Further, we observe enhanced Balmer absorption for many galaxies interior to this radius. This is consistent with an infall scenario where, after a starburst, Balmer absorption from young stars decays away over the course of ~ 1 Gyr, as the galaxy continues toward the cluster core. The radial distribution of enhanced-Balmer E+S0s

is consistent with the expected infall timescale of such galaxies. Galaxy mergers are not the source of this enhanced activity; the [OII] emitters reside in relatively low density regions, and do not appear to reside in groups. The small starbursts are likely caused by a rapidly acting physical process: possibilities include galaxy harassment and shocks in the ICM, perhaps generated by the sub-cluster merger in Cl 0024.

5) While the overall early type population is older in the cluster core than in the outskirts, we see trends with luminosity that indicate that smaller early types have more active star formation than larger ones. This seems to confirm evidence for downsizing seen by Treu et al. (2005a), and indicates that galaxy mass is a primary indicator of star formation activity, even as environmental effects work on top of this to produce radial variations in star formation. Both of these ultimately serve to decrease star formation toward the highest density regions, though the precise link to morphological transformation is still unclear because of the different timescales involved.

We have uncovered environmental processes working on cluster early types, but we have also seen variations in galaxy properties across the cluster that indicate that both galaxy mass and environment of initial formation are important in determining the overall assembly history of early type galaxies.

By obtaining high quality spectra of cluster members across a large area around Cl 0024, and combining with a panoramic *HST* mosaic, we have been able to uncover physical mechanisms at work that never would have been seen if we only looked at the cluster core. This underscores the importance of looking wide as well as far when attempting to understand how galaxies evolve within the large scale structure of the universe.

We thank Michael Cooper and Jeffery Newman for help with the DEIMOS data reduction pipeline, F. Owen, A. Metevier, and D. Koo for sharing redshifts, T. Kodama for allowing us access to H α equivalent widths and star formation rates from their survey, and J. Richard for assisting with DEIMOS observations in 2003. We thank M. Balogh, E. Ellingson, B. Holden, B. Poggianti, A. Babul and A. van der Wel for valuable discussions. Faint object spectroscopy at Keck Observatory is made possible with LRIS and DEIMOS thanks to the dedicated efforts of J. Cohen, P. Amico, S. Faber and G. Wirth. We acknowledge use of the Gauss-Hermite Pixel Fitting Software developed by R. P. van der Marel. The analysis pipeline used to reduce the DEIMOS data was developed at UC Berkeley with support from NSF grant AST-0071048. TT acknowledges financial support from a Hubble Fellowship grant HST-01.167.01. RSE acknowledges financial support from NSF grant AST-0307859 and STScI grants HST-GO-08559.01-A and HST-GO-09836.01-A.

REFERENCES

Abraham, R. G., van den Bergh, S. et al. 1996, ApJS, 107, 1
 Abraham, R. G., Smecker-Hane, T. A. et al. 1996, ApJ, 471, 694
 Balogh, M. L., Morris, S. L. et al. 1999, ApJ, 527, 54
 Balogh, M. L. & Morris, S. L. 2000, MNRAS, 318, 703
 Bamford, S.P., Milvang-Jensen, B., et al., 2005, MNRAS, in press
 Barr, J., Davies, R. et al., 2005, AJ, in press
 Bender, R., Burstein, D., Faber, S.M. 1993, ApJ, 411, 153
 Bender, R., Burstein, D., Faber, S.M. 1992, ApJ, 399, 462
 Bender, R., Saglia, R. P. et al. 1998, ApJ, 493, 529
 Bettoni, D., Galletta, G. & Garcia-Burillo, S. 2003, A&A, 405, 5
 Bower, R., Kodama, T., & Terlevich, A. 1998, MNRAS, 299, 1193
 Bower, R., Lucey, J.R., & Ellis, R.S. 1992, MNRAS, 254, 601
 Bressan, A., Chiosi, C., & Tantalo, R. 1996, A&A, 311, 425
 Burstein, D., Faber, S.M. 1984, ApJ, 399, 462
 Bruzual, G., & Charlot, S. 2003, MNRAS, 344, 1000
 Butcher, H., & Oemler, J., Jr. 1978, ApJ, 226, 559
 Couch, W. J., & Sharples, R. M. 1987, MNRAS, 229, 423
 Cowie, L.L., & Songaila, A. 1977, Nature, 266, 501
 Czoske, O., Kneib, J.-P., Soucail, G., et al. 2001, A&A, 372, 391
 Czoske, O., Moore, B., Kneib, J.-P., & Soucail, G. 2002, A&A, 386, 31

Davis, M. et al. 2003, SPIE, 4834, 161

Djorgovski, S. & Davis, M. 1987, ApJ, 313, 59

Dressler, A., 1980, ApJ, 236, 351

Dressler, A., & Gunn, J.E. 1983, ApJ, 270, 7

Dressler, A., Lynden-Bell, D., Burstein, D. et al. 1987, ApJ, 313, 42

Dressler, A., Oemler, A., Jr., Couch, W. J. et al. 1997, ApJ, 490, 577

Dressler, A., Smail, I., Poggianti, B. et al. 1999, ApJS, 122, 51

Ellingson, E. 2004, in "Outskirts of Galaxy Clusters: Intense Life in the Suburbs", IAU Colloquium 195, p.327-333

Evrard, A. E. 1991, MNRAS, 248, 8

Faber, S. M., Phillips, A.C., et al. 2003, Proc. SPIE, 4841, 1657

Fabricant, D., Franx, M., & van Dokkum, P. 2000, ApJ, 539, 577

Fasano, G., Poggianti, B.M. et al. 2000, ApJ, 542, 673

Fisher, D., Fabricant, D., Franx, M., & van Dokkum, P. 1998, ApJ, 498, 195

Fritz, A., Ziegler, B. et al. 2005, MNRAS, 358, 233

Furlanetto, S. R., & Loeb, A. 2004, ApJ, 611, 642

Gerhard, O., Kronawitter, A. et al. 2001, AJ, 121, 1936

Gerken, B., Ziegler, B., et al. 2004, A&A, 421, 59

Gill, S. P., Knebe, A. & Gibson, B., 2005, MNRAS, 356, 1327

Gómez, P.L., Nichol, R. C. et al. 2003, ApJ, 584, 210

Homeier, N.L., Demarco, R. et al. 2005, ApJ, 621, 651

Holden, B.P., van der Wel, A. et al. 2005, ApJL, 620, L83

Horne, K. 1986, PASP, 98, 609

Jørgensen, I., Franx, M., & Kjærgaard, P. 1995a, MNRAS, 276, 1341

Jørgensen, I., Franx, M., & Kjærgaard, P. 1995b, MNRAS, 273, 1097

Jørgensen, I., Franx, M., & Kjærgaard, P. 1996, MNRAS, 280, 167

Kelson, D. D., Illingworth, G. D., van Dokkum, P. G., & Franx, M. 2000a, ApJ, 531, 137

Kelson, D. D., Illingworth, G. D., van Dokkum, P. G., & Franx, M. 2000b, ApJ, 531, 184

Kelson, D.D., Illingworth, G.D. et al. 2001, ApJ, 552, L17

Kennicut, R. C., Jr. 1992, ApJ, 388, 310

Kneib, J-P., Hudelot, P. et al. 2003, ApJ, 598, 804

Kodama, T., Smail, I., Nakata, F., Okamura, S., Bower, R. G. 2001, ApJ, 562, 9

Kodama, T., Balogh, M. et al. 2004, MNRAS, 354, 1103

Kuntschner, H. 2000, MNRAS, 315, 184

Kuntschner, H., Lucey, J.R. et al. 2001, MNRAS, 323, 615

Lewis, I., Balogh, M. et al., 2002, MNRAS, 334, 673

Lucey, J.R., Guzmán, R., et al. 1991, MNRAS, 253, 584

Menanteau, F., Ford, H.C. et al. 2004, ApJ, 612, 202

Metevier, A.J. & Koo, D. C., 2004, IAUS, 220, 415

Milvang-Jensen, B., Aragón-Salamanca, A., et al., 2003, MNRAS, 339, L1

Moore, B., Katz, N. et al. 1996, Nature, 379, 613

Moore, B., Lake, G. et al. 1999, MNRAS, 304, 465

Moore, B., Lake, G., & Katz, N. 1998, ApJ, 495, 139

Nulson, P. E. J. 1982, MNRAS, 198, 1007

Peng, C. Y., Ho, L. C., Impey, C. D., & Rix, H. 2002, AJ, 124, 266

Poggianti, B. M., Smail, I., Dressler, A. et al. 1999, ApJ, 518, 576

Poggianti, B. M., Bridges, T.J. et al. 2004, ApJ, 601, 197

Postman, M., Franx, M. et al. 2005, in press (astro-ph/0501224)

Postman, M., Lauer, T. R. et al. 1998, ApJ, 506, 33

Quilis, V., Moore, B., & Bower, R. 2000, Science, 288, 1617

Roettiger, K., Burns, J., & Loken, C. 1996, ApJ, 473, 651

Ruderman, J.T. & Ebeling, H. 2005, ApJ, 623, 81

Rusin, D., Kochanek, C. S. et al., 2003, ApJ, 587, 143

Ryu, D., Kang, H. et al. 2003, ApJ, 593, 599

Saglia, R.P., Bender, R., & Dressler, A., 1993, A&A, 279, 75

Schlegel, D.J., Finkbeiner, D. P., & Davis, M. 1998, ApJ, 500, 525

Smail, I., Dressler, A., Couch, W. J. et al. 1997, ApJS, 110, 213

Smith, G. P., Treu, T., et al. 2005, ApJ, 620, 78

Tantalo, R. & Chiosi, C. 2004, MNRAS, 353, 917

Thomas, D., Maraston, C., & Bender, R. 2003, MNRAS, 339, 897

Tonizatto, T. & Schindler, S. 2001, MNRAS, 325, 509

Trager, S. C., Worthey, G., et al. 1998, ApJS116, 1

Treu, T., Ellis, R. S., et al., 2005b, ApJ, in press (astro-ph/0503164)

Treu, T., Ellis, R. S., et al., 2005a, ApJL, 622, 5

Treu, T., Ellis, R. S., et al., 2003, ApJ, 591, 53

Treu, T., Stiavelli, M., Casertano, S., et al. 2002, ApJ, 564, L13

Treu, T., Stiavelli, M., Møller, P., et al. 2001b, MNRAS, 326, 221

Treu, T., Stiavelli, M., Bertin, G., et al. 2001a, MNRAS, 326, 237

Treu, T., Stiavelli, Casertano, S., et al., 1999, MNRAS, 308, 1037

Van der Marel, R., 1994 MNRAS, 270, 271

van der Wel, A., Franx, M., et al. 2005, ApJ, in press (astro-ph/0502228)

van Dokkum, P. & Franx, M. 1996, MNRAS, 281, 985

van Dokkum, P. & Franx, M. 2001, ApJ, 533, 90

Whitmore, B. C., Gilmore, D. M. & Jones, C. 1993, ApJ, 407, 489

Worley, G., Faber, S.M., et al. 1994, ApJS, 94, 687

Worley, G. & Ottaviani, D. 1997, ApJS, 111, 377

Wuyts, S., van Dokkum, P. G., Kelson, D. D., et al. 2004, ApJ, 605, 677

Zhang, Y. -Y., Bøhringer, H., et al. 2005, A&A, 429, 85

Ziegler, B.L., Thomas, D. et al. 2005, A&A, 433, 519

Ziegler, B.L., Böhm, A., et al. 2003, ApJ, 598, L87

Ziegler, B.L., Bower, R.G., et al. 2001, MNRAS, 325, 1571

TABLE 1
 OBSERVED E+S0 CLUSTER MEMBERS

Object	α ($^{\circ}$)	δ ($^{\circ}$)	z	F814W (mag)	R (Mpc)	Σ_{10} (Mpc $^{-2}$)	Morph
p0i102c3	6.65796	17.16050	0.3897	19.42	0.14	255	S0
p0i139c3	6.66004	17.16630	0.3974	20.15	0.19	300	E/S0
p0i15c3	6.64000	17.15560	0.3984	19.84	0.27	195	S0
p0i170c3	6.64412	17.17120	0.3931	19.24	0.22	214	E
p0i1c3	6.65400	17.15350	0.3940	20.23	0.20	257	E/S0
p0i1c4	6.66014	17.15402	0.3967	20.54	0.25	212	E
p0i206c3	6.64763	17.16280	0.3972	18.51	0.07	951	E
p0i209c3	6.64012	17.16750	0.3893	21.76	0.24	214	S0
p0i217c3	6.65629	17.16270	0.3912	20.18	0.10	254	E/S0
p0i24c2	6.65271	17.14714	0.3954	21.11	0.32	204	E/S0
p0i38c4	6.66325	17.15350	0.3860	20.36	0.30	244	S0
p0i39c3	6.64025	17.15860	0.3919	19.62	0.23	265	S0
p0i3c3	6.65633	17.15240	0.3915	19.64	0.24	255	S0
p0i42c3	6.65792	17.15610	0.3994	18.85	0.19	390	E
p0i45c2	6.65133	17.14800	0.3951	21.46	0.30	183	S0
p0i49c2	6.64896	17.14980	0.3946	19.26	0.27	200	S0
p0i4c4	6.65950	17.15350	0.3910	20.95	0.25	212	E
p0i53c4	6.67150	17.16720	0.3976	18.88	0.41	102	E
p0i55c2	6.64754	17.14220	0.3960	19.91	0.43	206	S0
p0i66c3	6.65321	17.15800	0.3843	20.01	0.11	372	S0
p0i72c3	6.64875	17.16200	0.3920	18.11	0.05	1024	E
p0i79c3	6.65000	17.16280	0.3883	17.75	0.02	637	E
p0i85c3	6.65663	17.15780	0.3943	19.02	0.15	339	E
p0i91c3	6.64575	17.17260	0.3887	19.57	0.23	151	E
p0i95c3	6.64313	17.17280	0.3876	18.77	0.26	274	E
p10i1c2	6.78233	17.18040	0.3967	18.66	2.59	14	S0
p11i147c4	6.72475	17.17760	0.3955	20.36	1.47	16	S0
p12i160c2	6.67425	17.19140	0.3951	20.40	0.74	44	E
p12i160c3	6.64088	17.20460	0.3955	19.79	0.88	88	E/S0
p12i168c4	6.65725	17.23670	0.3800	21.55	1.52	20	E/S0
p12i173c4	6.66853	17.23410	0.3962	20.14	1.50	22	S0
p13i130c3	6.62154	17.23410	0.3934	21.98	1.57	25	E/S0
p13i133c4	6.59632	17.20980	0.3967	21.42	1.45	57	E
p13i135c4	6.59546	17.20870	0.3965	18.61	1.44	56	S0
p13i1c4	6.60596	17.22300	0.3975	19.88	1.52	34	E
p13i25c2	6.58954	17.23660	0.3962	19.59	1.94	17	S0
p13i78c4	6.61300	17.20720	0.3973	18.93	1.18	109	E
p13i86c4	6.60258	17.21320	0.3929	22.27	1.41	60	E/S0
p14i2c2	6.55800	17.22640	0.3933	20.61	2.25	13	E
p15i144c4	6.47717	17.27400	0.3967	19.99	4.10	7	S0
p17i2c4	6.75733	17.13590	0.3941	20.92	2.15	8	S0
p18i43c2	6.72658	17.14080	0.3925	19.01	1.54	31	E
p18i51c2	6.72458	17.14120	0.3933	19.87	1.50	26	E
p18i66c3	6.71600	17.14440	0.3934	19.98	1.32	26	E
p19i1c3	6.58353	17.17150	0.3939	20.48	1.34	18	E/S0
p19i75c4	6.60362	17.17270	0.3941	21.41	0.96	38	E/S0
p19i92c2	6.57613	17.15490	0.3811	21.15	1.48	22	E/S0
p20i35c4	6.53687	17.16520	0.3971	19.42	2.24	8	S0
p20i48c3	6.54025	17.18710	0.3921	20.12	2.23	7	E
p24i115c3	6.61158	17.09930	0.4082	21.65	1.52	19	S0
p24i1c3	6.63138	17.10100	0.3981	18.87	1.33	26	E/S0
p24i42c4	6.63029	17.11800	0.4018	20.64	1.01	42	E
p24i79c4	6.64067	17.11160	0.3927	20.64	1.07	35	E
p24i87c3	6.62296	17.10520	0.3972	19.32	1.30	26	S0
p25i29c3	6.57688	17.11700	0.3924	20.32	1.73	14	E
p25i193c3	6.58088	17.11730	0.3970	19.21	1.66	19	S0
p27i174c3	6.46279	17.14510	0.3978	19.06	3.71	5	S0
p27i9c2	6.44396	17.14130	0.3792	21.89	4.09	5	E/S0
p28i87c2	6.73458	17.02130	0.3950	20.64	3.33	9	E
p35i112c2	6.51850	17.33350	0.3833	20.12	4.36	21	S0
p35i143c2	6.49954	17.33630	0.3951	19.94	4.64	15	S0
p35i143c3	6.52433	17.32190	0.3927	19.13	4.10	33	E
p35i16c3	6.51429	17.31730	0.3946	18.85	4.15	23	E
p35i178c2	6.51071	17.32570	0.3931	19.23	4.33	21	S0
p35i182c3	6.52896	17.32850	0.3956	19.28	4.16	23	S0
p36i106c3	6.61754	17.19870	0.3970	22.05	0.99	72	S0
p36i146c3	6.60642	17.20250	0.3987	19.72	1.20	118	S0
p36i182c2	6.62129	17.17350	0.3959	19.28	0.63	169	S0
p36i182c3	6.60512	17.19650	0.3930	20.65	1.14	106	S0
p36i184c2	6.61846	17.18120	0.3955	19.19	0.75	114	S0
p36i187c3	6.60879	17.19940	0.3965	20.17	1.12	126	E/S0
p36i1c4	6.63014	17.20229	0.3907	19.45	0.91	77	E/S0
p36i2c2	6.63088	17.18210	0.3958	18.01	0.56	99	E
p36i2c3	6.61833	17.18800	0.3922	19.92	0.83	130	S0

TABLE 1
OBSERVED E+S0 CLUSTER MEMBERS

p36i31c4	6.63221	17.20670	0.3905	18.73	0.97	123	E
p36i32c4	6.63254	17.19910	0.3916	20.14	0.83	117	S0
p36i34c2	6.63088	17.17420	0.3950	20.91	0.46	124	S0
p36i36c4	6.63254	17.19970	0.3949	20.96	0.84	121	E
p36i3c2	6.62933	17.18590	0.3931	20.22	0.64	105	E
p36i48c3	6.61658	17.19380	0.3934	19.74	0.93	103	S0
p36i5c2	6.63542	17.17390	0.3969	19.18	0.39	186	S0
p36i67c4	6.64803	17.20200	0.3951	20.87	0.81	65	E/S0
p36i70c4	6.64450	17.20400	0.3975	20.38	0.86	75	E
p36i71c3	6.60769	17.20461	0.3996	21.25	1.21	105	E/S0
p36i76c2	6.62469	17.16852	0.3959	20.29	0.53	151	S0
p36i76c3	6.60667	17.20060	0.3932	19.95	1.17	124	S0
p36i89c2	6.62292	17.17570	0.3977	19.97	0.62	154	S0
p37i110c2	6.68208	17.12020	0.3954	20.86	1.06	30	S0
p37i122c2	6.69346	17.10380	0.3918	21.69	1.47	16	E/S0
p37i16c4	6.68229	17.13830	0.3975	18.02	0.79	81	S0
p37i206c4	6.68004	17.14495	0.3965	20.44	0.67	87	E
p37i207c4	6.68607	17.14283	0.3953	21.47	0.80	146	S0
p37i64c4	6.66879	17.14430	0.3977	20.18	0.51	72	E/S0
p37i9c4	6.66721	17.13930	0.3999	20.81	0.57	60	S0
p38i1c4	6.62454	17.14090	0.4003	20.39	0.69	55	E
p38i76c4	6.62533	17.13030	0.3976	20.88	0.84	37	S0
p3i72c2	6.63067	17.32760	0.4007	20.67	3.40	7	S0
p5i9c3	6.74192	17.26600	0.3904	20.69	2.76	10	E/S0
p7i128c3	6.63150	17.28690	0.3934	19.85	2.57	72	S0
p7i133c3	6.63194	17.28540	0.3967	20.82	2.54	52	S0
p7i136c3	6.63197	17.28490	0.3960	19.93	2.53	52	S0
p7i1c2	6.60829	17.28990	0.3981	18.64	2.74	24	E
p7i67c3	6.62904	17.28590	0.3961	20.60	2.56	71	S0
p9i20c3	6.83968	17.16743	0.3953	19.01	3.69	9	S0

NOTE. — Object names are abbreviated from those given in Paper I, which listed objects by WFPC2 pointing, WFPC2 chip, and ID number. For example, p0i102c3 refers to object number 102 on chip 3, from pointing 0. Right ascension (α) and declination (δ) are for epoch J2000. F814W magnitudes are corrected for galactic extinction, adopting $E(B-V) = 0.057$ (Schlegel et al. 1998). R and Σ_{10} denote, respectively, the projected radius and local density of each galaxy, calculated according to the method described in the text. Typical uncertainty in Σ_{10} is 25%, equal to the rms variation in the local density across different measurement methods. Errors in F814W magnitudes are less than 0.05 mag rms; more information on photometric measurements is given in Paper I.

TABLE 3
ALL MEASUREMENTS OF OBSERVED E+S0 MEMBERS

Object	OII (Å)	H δ_A (Å)	H γ_A (Å)	Mg ^b (Å)	Fe5270 (Å)	Fe5335 (Å)	σ_0 (km s ⁻¹)	$\langle \mu_V \rangle$ (mag '' ⁻²)	R_e ('')	Å^{-1}	S/N Observed
p0i102c3	-0.3	-0.1	-4.1	4.7	2.2	2.4	154 ± 10	21.13	1.3		23.4
p0i139c3	0.0	-0.4	-2.8	4.0	2.8	2.8	$140. \pm 7$	18.85	0.3		16.7
p0i15c3	0.0	-3.2	-6.3	4.7	2.2	1.3	278 ± 26	20.30	0.7		12.3
p0i170c3	0.0	-1.3	-3.2	4.8	1.5	1.9	185 ± 13	—	—		26.6
p0i1c3	-0.3	3.3	-1.4	4.0	2.0	3.3	105 ± 19	20.61	0.5		6.9
p0i1c4	-0.5	0.5	-2.0	—	2.6	2.5	69 ± 10	19.72	0.4		11.9
p0i206c3	-0.1	0.0	-5.6	1.2	0.7	1.2	491 ± 22	19.87	1.2		19.9
p0i209c3	0.0	-5.0	-6.5	2.7	2.8	0.9	—	—	—		1.6
p0i217c3	0.0	-1.3	-5.6	4.2	2.3	1.9	144 ± 11	19.55	0.4		14.0
p0i24c2	0.0	0.0	-6.3	2.2	3.2	2.7	165 ± 24	18.97	0.2		8.2
p0i38c4	0.0	-0.6	-9.0	3.9	3.6	0.1	—	—	—		6.5
p0i39c3	0.0	0.3	-4.7	6.7	2.4	2.6	204 ± 22	20.20	0.8		16.3
p0i3c3	0.0	-2.5	-5.6	4.2	1.8	1.8	$300. \pm 31$	19.22	0.5		24.4
p0i42c3	0.0	-0.4	-4.7	4.3	2.9	2.3	252 ± 18	19.55	0.9		40.9
p0i45c2	-10.1	6.4	-5.6	0.1	3.4	3.3	—	—	—		6.6
p0i49c2	0.0	-1.6	-3.8	2.8	1.4	2.3	236 ± 16	20.75	1.2		22.5
p0i4c4	-0.8	-0.6	-1.1	3.8	3.0	2.3	128 ± 13	20.28	0.4		9.5
p0i53c4	0.0	-1.8	-2.0	3.2	1.1	0.9	403 ± 32	20.00	1.2		17.2
p0i55c2	0.0	5.9	1.1	—	2.9	0.8	—	—	—		5.8
p0i66c3	-6.0	-0.3	-4.0	3.2	3.6	2.4	86 ± 7	21.15	1.1		15.3
p0i72c3	0.0	-1.9	-5.8	4.6	2.4	2.3	275 ± 23	—	—		42.2
p0i79c3	0.0	-1.2	-5.4	5.4	2.1	2.5	283 ± 23	21.08	3.1		28.5
p0i85c3	-1.7	-0.4	-5.4	2.4	0.5	0.1	425 ± 49	20.61	1.4		20.8
p0i91c3	0.0	-2.2	-3.1	5.6	2.9	2.5	169 ± 15	19.01	0.4		24.8
p0i95c3	0.0	-1.3	-6.3	4.9	2.7	1.9	221 ± 24	19.36	0.8		36.9
p10i1c2	-0.4	-0.2	-4.6	2.3	2.5	2.8	214 ± 13	19.52	0.8		38.4
p11i47c4	0.0	-1.0	-2.3	7.6	3.3	3.1	126 ± 7	19.42	0.4		18.9
p12i160c2	-0.7	6.0	-1.1	6.4	2.9	3.5	—	—	—		6.0
p12i160c3	0.0	0.4	0.6	6.5	3.4	3.0	138 ± 19	19.84	0.6		8.7
p12i168c4	-28.7	1.4	2.2	2.3	2.3	4.0	—	—	—		4.8
p12i73c4	-2.3	-0.2	-3.2	—	—	—	132 ± 12	20.07	0.6		12.3
p13i30c3	-38.9	1.1	—	—	-0.3	7.2	—	—	—		2.1
p13i133c4	0.0	-0.3	-4.5	—	—	—	—	—	—		4.0
p13i135c4	-2.7	-0.6	-3.6	3.4	1.8	2.2	143 ± 11	21.21	1.6		17.1
p13i1c4	-1.4	-3.0	-5.7	8.4	—	—	143 ± 22	20.37	0.8		8.4
p13i25c2	0.0	-0.3	-5.0	1.1	2.6	2.8	147 ± 8	19.74	0.6		23.4
p13i78c4	-0.2	-0.1	-1.6	—	2.5	2.0	232 ± 21	19.72	0.8		19.6
p13i86c4	-25.1	7.5	-0.7	—	—	—	—	—	—		2.5
p14i2c2	-7.7	2.0	-0.4	6.1	1.4	1.5	119 ± 13	21.22	0.8		12.5
p15i144c4	-0.8	1.9	-5.0	—	0.7	2.9	$130. \pm 11$	19.71	0.5		12.4
p17i2c4	-3.9	-0.9	0.6	2.7	3.4	5.2	—	—	—		6.4
p18i43c2	0.0	-0.9	-4.4	4.3	1.8	2.4	234 ± 21	19.94	1.0		32.6
p18i51c2	0.0	-0.1	0.4	—	2.1	1.5	152 ± 10	18.93	0.3		18.9
p18i66c3	0.0	-1.6	-4.9	4.2	2.3	2.0	168 ± 14	18.62	0.3		20.8
p19i1c3	-0.7	0.0	-6.0	—	—	—	—	—	—		7.0
p19i75c4	-1.8	2.7	-0.5	5.4	0.0	1.6	—	—	—		5.0
p19i92c2	-49.9	3.4	-1.8	2.2	-0.6	0.4	—	—	—		6.8
p20i35c4	-6.5	0.3	-0.7	1.6	1.8	2.0	175 ± 11	19.41	0.5		25.1
p20i48c3	0.0	-1.3	-4.0	3.9	2.5	0.5	172 ± 11	19.23	0.4		10.0
p24i115c3	-43.1	3.8	—	9.0	1.2	-0.2	—	—	—		4.5
p24i41c3	-0.5	2.8	1.1	1.9	-0.7	0.9	144 ± 16	20.44	1.2		12.4
p24i42c4	0.0	-4.9	-1.1	1.7	2.6	-1.2	—	—	—		5.6
p24i79c4	0.0	-0.8	3.9	2.6	1.0	1.1	—	—	—		4.8
p24i87c3	0.0	-2.4	-6.3	3.8	1.8	0.7	153 ± 8	19.75	0.7		11.0
p25i29c3	-0.7	-0.2	-2.5	3.2	2.8	2.9	152 ± 16	18.36	0.2		13.4
p25i93c3	-30.1	-1.2	-2.3	2.8	3.0	2.2	—	—	—		5.5
p27i174c3	0.0	0.2	-3.4	5.0	2.7	1.9	187 ± 17	19.64	0.8		24.8
p27i9c2	-29.8	-3.2	3.8	2.7	—	-1.7	—	—	—		3.9
p28i87c2	-46.5	2.4	-2.2	1.8	0.5	1.2	—	—	—		7.4
p35i112c2	0.0	-1.4	-0.3	3.9	2.5	1.7	71 ± 8	—	—		9.6
p35i143c2	0.0	-4.0	-9.6	5.4	2.8	2.7	148 ± 9	18.99	0.4		19.8
p35i43c3	-4.4	-0.9	-4.4	3.6	3.0	2.5	$170. \pm 12$	20.36	1.1		18.2
p35i16c3	0.0	-1.1	-5.0	4.2	2.5	2.9	220 ± 12	19.11	0.7		27.0
p35i78c2	-17.0	-1.6	-4.5	3.5	1.4	2.2	191 ± 13	19.36	0.6		36.1
p35i82c3	0.0	-0.7	-5.1	4.9	2.3	2.4	201 ± 16	19.62	0.7		36.4
p36i106c3	0.0	3.1	-3.0	—	—	—	—	—	—		3.0
p36i146c3	0.0	-1.2	7.1	3.4	2.2	3.0	167 ± 12	20.15	0.7		12.5
p36i182c2	0.0	-0.6	-4.4	2.6	2.2	2.4	$130. \pm 6$	20.09	0.9		26.6
p36i182c3	-6.6	2.4	-1.0	—	7.6	1.5	108 ± 24	20.93	0.7		6.8
p36i184c2	-0.5	-2.5	-3.4	4.9	1.6	2.7	165 ± 10	20.00	0.9		27.2
p36i187c3	-2.9	-0.2	4.9	4.4	1.3	3.1	123 ± 10	19.80	0.5		8.8
p36i1c4	-3.3	-0.6	-4.2	4.1	2.9	2.5	79 ± 10	19.12	0.5		22.2
p36i2c2	0.0	-1.7	-5.1	2.0	2.1	1.6	376 ± 24	20.42	1.8		22.6
p36i2c3	-2.6	1.3	6.5	6.8	3.0	2.5	164 ± 10	21.76	1.5		16.2

TABLE 3
ALL MEASUREMENTS OF OBSERVED E+S0 MEMBERS

p36i31c4	0.0	-3.1	-4.1	4.4	2.0	1.6	264 ± 28	20.14	1.1	32.6
p36i32c4	0.0	-3.1	-3.4	4.5	2.9	3.1	215 ± 19	19.48	0.4	7.6
p36i34c2	0.0	-1.1	-5.0	—	1.7	2.6	114 ± 10	19.52	0.3	10.4
p36i36c4	-5.9	0.0	-9.5	4.7	1.3	0.8	—	—	—	5.8
p36i3c2	0.0	-0.4	-8.9	2.3	2.6	2.2	$110. \pm 9$	19.64	0.5	15.3
p36i48c3	-1.4	-4.1	-8.1	7.1	1.9	2.1	188 ± 15	19.97	0.6	12.8
p36i5c2	-6.8	2.1	-2.1	0.3	2.5	1.7	169 ± 15	20.41	1.2	12.5
p36i67c4	-14.3	1.0	-0.8	4.4	—	—	—	—	—	7.0
p36i70c4	-8.7	2.0	-0.9	2.3	2.6	1.6	83 ± 8	19.55	0.4	18.5
p36i71c3	-4.7	1.1	-4.2	4.3	1.3	1.4	—	—	—	7.3
p36i76c2	-4.5	0.1	0.7	4.3	2.8	2.7	261 ± 13	20.12	0.5	13.2
p36i76c3	-2.8	3.0	-2.0	5.7	0.3	0.9	87 ± 14	20.93	1.1	9.8
p36i89c2	-4.0	1.2	0.4	—	2.1	2.2	107 ± 10	21.14	1.1	14.9
p37i110c2	0.0	2.7	-3.5	7.3	3.2	3.2	114 ± 8	19.67	0.3	10.5
p37i122c2	-41.3	0.8	-3.4	2.0	1.7	1.4	—	—	—	4.0
p37i16c4	-1.6	1.5	-2.5	3.7	2.2	1.9	233 ± 11	19.86	1.4	55.1
p37i206c4	0.0	0.5	-7.3	—	2.7	2.7	64 ± 6	19.12	0.3	14.5
p37i207c4	0.0	-0.8	12.5	7.8	2.2	1.8	—	—	—	1.8
p37i64c4	-1.3	1.1	1.2	4.6	1.7	-2.3	254 ± 45	18.86	0.3	7.1
p37i9c4	-5.9	2.1	-1.3	0.4	3.1	1.2	—	—	—	10.1
p381c4	-0.9	-2.9	-0.4	—	-0.8	2.1	—	—	—	5.5
p38i76c4	0.0	5.6	-8.5	—	0.5	1.6	—	—	—	6.7
p3i72c2	-7.9	0.5	-6.8	0.8	6.9	5.9	—	—	—	2.8
p5i9c3	-0.7	-0.3	-1.9	4.2	2.0	2.3	$100. \pm 10.$	18.93	0.2	14.3
p7i128c3	0.0	-0.8	-5.0	3.4	2.3	2.5	204 ± 14	—	—	27.2
p7i133c3	0.0	-1.3	-3.6	—	3.4	-0.6	161 ± 21	21.12	0.7	7.7
p7i136c3	0.0	0.2	-4.4	2.3	3.4	1.9	168 ± 10	20.08	0.7	18.4
p7i1c2	-6.4	-1.5	-6.9	3.6	2.2	2.5	222 ± 14	19.75	1.0	46.8
p7i67c3	0.0	1.0	-3.6	9.9	2.6	3.2	127 ± 8	19.44	0.3	16.5
p9i20c3	-6.1	0.3	-3.6	3.3	3.2	2.1	112 ± 10	21.29	1.6	22.3

NOTE. — Line strengths are given in Å of equivalent width, with negative values denoting emission, and positive values indicating absorption. No aperture corrections have been applied to the indices. σ_0 lists velocity dispersions, when measured, and the values are aperture-corrected to a 3''.4 diameter aperture at the distance to the Coma cluster. $\langle \mu_V \rangle$ indicates the mean surface brightness within the effective radius, R_e , in rest frame V-band, and is corrected for cosmological dimming. Typical errors on line indices are less than $\pm 0.2 \text{ Å}$ on $H\delta_A$ and $H\gamma_A$, and $\pm 0.1 \text{ Å}$ on [OII], Mg^b , Fe5270, and Fe5335. Errors on μ_V and R_e are 0.1 mag and 0''.1, respectively.